STRUCTURAL BASIS OF TRANSCRIPTION INHIBITION BY FIDAXOMICIN (LIPIARMYCIN A3)

Wei Lin[1,*], Kalyan Das[2,*,**], David Degen[1,*], Abhishek Mazumder[1], Diego Duchi[3], Dongye Wang[1], Yon W. Ebright[1], Richard Y. Ebright[1], Elena Sineva[1], Matthew Gigliotti[1], Aashish Srivastava[1], Sukhendu Mandal[1], Yi Jiang[1], Yu Liu[1], Ruiheng Yin[1], Zhening Zhang[4], Edward T. Eng[4], Dennis Thomas[5], Stefano Donadio[6], Haibo Zhang[7], Changsheng Zhang[7], Achillefs N. Kapanidis[3], and Richard H. Ebright[1,* *,***]

[1]Waksman Institute and Department of Chemistry, Rutgers University, Piscataway NJ 08854, USA

[2]Rega Institute and Department of Microbiology and Immunology, KU Leuven, 3000 Leuven, Belgium

[3]Department of Physics, University of Oxford, Oxford OX1 3PU, United Kingdom

[4]The National Resource for Automated Molecular Microscopy, Simons Electron Microscopy Center, New York Structural Biology Center, New York NY 10027, USA

[5]Center for Integrative Proteomics, Rutgers University, Piscataway NJ 08854, USA

[6]NAICONS Srl., 20139 Milan, Italy

[7]South China Sea Institute of Oceanology, Chinese Academy of Sciences, Guangzhou 510301, China

*Contributed equally

**Corresponding authors: kalyan.das@kuleuven.be, ebright@waksman.rutgers.edu

***Lead contact: ebright@waksman.rutgers.edu

SUMMARY

Fidaxomicin is an antibacterial drug in clinical use in treatment of *Clostridium difficile* diarrhea. The active ingredient of the antibacterial drug fidaxomicin, lipiarmycin A3 (Lpm), functions by inhibiting bacterial RNA polymerase (RNAP). Here, we report a cryo-EM structure of *Mycobacterium tuberculosis* RNAP holoenzyme in complex with Lpm at 3.5 Å resolution. The structure shows that Lpm binds at the base of the RNAP "clamp." The structure exhibits an open conformation of the RNAP clamp, suggesting that Lpm traps an open-clamp state. Single-molecule fluorescence-resonance-energy-transfer experiments confirm that Lpm traps an open-clamp state and define effects of Lpm on clamp dynamics. We suggest that Lpm inhibits transcription by trapping an open-clamp state, preventing simultaneous interaction with promoter -10 and -35 elements. The results account for the absence of cross-resistance between Lpm and other RNAP inhibitors, account for structure-activity relationships of Lpm derivatives, and enable structure-based design of improved Lpm derivatives.

INTRODUCTION

Fidaxomicin is an antibacterial drug in clinical use in treatment of *Clostridium difficile* diarrhea (Lancaster and Matthews, 2012; Venugopal and Johnson, 2012). The active pharmaceutical ingredient of fidaxomicin, lipiarmycin A3 (Lpm; Kaufmann et al., 2015; Serra et al., 2017; Fig. S1A), is a macrocyclic antibiotic with bactericidal activity against Gram-positive bacteria and efflux-deficient strains of Gram-negative bacteria (Lancaster and Matthews, 2012; Venugopal and Johnson, 2012; Srivastava et al., 2011). Lpm functions by inhibiting bacterial RNA polymerase (RNAP; Talpaert et al., 1975; Sonenshein et al., 1977; Sonenshein and Alexander, 1979). Lpm exhibits no cross-resistance with the classic RNAP inhibitor rifampin (Rif; Sonenshein et al., 1977; Ebright, 2005) and inhibits transcription initiation at an earlier step than Rif (Sonenshein et al., 1977; Ebright, 2005; Tupin et al., 2010; Artsimovitch et al., 2012),

suggesting that the binding site and mechanism of Lpm differ from those of Rif. Efforts spanning more than a decade to obtain structural information on RNAP-Lpm by use of X-ray crystallography have been unsuccessful.

RESULTS AND DISCUSSION

Structure of *Mtb* RNAP-Lpm

Structural information on RNAP is available for three bacterial genera: the Gram-positive bacterial genus *Mycobacterium* (Hubin et al., 2017; Lin et al., 2017), the Gram-negative bacterial genus *Escherichia* (Murakami et al., 2013), and the *Thermus/Deinococcus*-clade bacterial genus *Thermus* (Zhang et al., 1999; Vassylyev et al., 2002). Lpm potently inhibits RNAP from genus *Mycobacterium* and genus *Escherichia* (IC50s = 0.3 μM and 8 μM, respectively; Talpaert et al., 1975; Kurabachew, 2008; Fig. S1B), but only poorly inhibits RNAP from genus *Thermus* (IC50 = 200 μM; Fig. S1B). Accordingly, efforts in our laboratory to obtain structural and functional information on RNAP-Lpm focussed on RNAP from genus *Mycobacterium* and genus *Escherichia*.

We first sought to obtain structural information on RNAP-Lpm by use of X-ray crystallography. However, we were unable to prepare crystals of RNAP-Lpm, despite numerous attempts at crystal soaking (assessing all reported crystal forms of RNAP from genus *Mycobacterium* and genus *Escherichia*) and co-crystallization (assessing crystallization conditions for all reported crystal forms of RNAP from genus *Mycobacterium* and genus *Escherichia,* and assessing $>10^4$ additional crystallization conditions by robotic screening).

We then sought to obtain structural information on RNAP-Lpm by use of cryo-EM with single-particle reconstruction (Merino and Raunser, 2017; Boland et al., 2017). Pilot experiments suggested that cryo-EM particle-orientation distributions using RNAP from genus *Mycobacterium* were more favorable for high-resolution structure determination than cryo-EM particle-orientation distributions

using RNAP from genus *Escherichia.* Accordingly, our cryo-EM analysis focussed on RNAP from genus *Mycobacterium.*

We determined a structure of *Mycobacterium tuberculosis* (*Mtb*) RNAP σ^A holoenzyme in complex with Lpm by use of cryo-EM with single-particle reconstruction (Merino and Raunser, 2017; Boland et al., 2017) (Figs. 1, S1-S3). The cryo-EM density map shows unambiguous density for RNAP, including the taxon-specific, *Mycobacterium*-specific sequence insertion (β′*Mtb*SI or "gate"; Lin et al., 2017), for σ conserved regions 2, 3, and 4 (σR2, σR3, and σR4), and for Lpm. The mean resolution of the structure is 3.5 Å (Fig. S1F). Local resolution ranges from ~2.5-3.8 Å in central parts of the structure, including RNAP residues close to Lpm, to ~5-6.5 Å in peripheral parts of the structure, including β′*Mtb*SI and σR4 (Figs. 1a, S1G, S2A). Local B-factors range from ~8-100 $Å^2$ in central regions to ~300-400 $Å^2$ in peripheral regions (Fig. 2B). The map show clear density for backbone and sidechain atoms of RNAP and individual functional groups of Lpm (Fig. S2C-D).

The cryo-EM structure shows that the Lpm binding site is located at the base of the RNAP clamp (Landick, 2001; Cramer et al., 2001; Chakraborty et al., 2012) and encompasses RNAP clamp α-helices βa16α1 and β′a4α1 and RNAP switch-region (Cramer et al., 2001; Srivastava et al., 2011) switches SW2, SW3, and SW4 (Figs. 1, S3). Lpm binds to RNAP in a fully-extended conformation similar to conformations in crystal structures of Lpm alone (Fig. S3A). All five structural moieties of Lpm--isobutyryl, β-D-noviosyl, macrocycle, β-D-rhamnosyl, and homodichloro-orsellinyl--interact with RNAP (Figs. 1D-E, S1A, S3B-C). Lpm makes H-bonds with six RNAP residues: βT1096 (V1298), βK1101 (K1303), β′R84 (Q94), β′R89 (R99), β′E323 (D248), and β′R412 (R337) [residues numbered as in *Mtb* RNAP (UniProtKB: P9WGY9, UniProtKB: P9WGY7) and, in parentheses, as in *Escherichia coli* RNAP (UniProtKB: P0A8V2, UniProtKB: P0A8T7)]. Alanine substitutions of five of these RNAP residues results in Lpm-resistance, confirming the interactions are functionally relevant (Fig. S3D).

Sequence alignments show that residues of RNAP that contact Lpm are conserved in Gram-positive and Gram-negative bacterial RNAP, but are not conserved in human RNAP I, II, and III

(Fig. S4A-B), accounting for the ability of Lpm to inhibit both Gram-positive and Gram-negative bacterial RNAP but not human RNAP I, II, and III (Fig. S4C).

The cryo-EM structure accounts for structure-activity relationships of Lpm analogs produced by metabolism (Babakhani et al., 2011), precursor feeding (Hochlowski et al., 1997), mutasynthesis (Xiao et al., 2011; Niu et al., 2011), and semi-synthesis (Figs. 1D-E, S3B-C, S5). The structure accounts for structure-activity relationships indicating functional importance of the Lpm isobutyryl moiety ("b1" vs. Lpm), β-D-noviosyl moiety ("c1" vs. "b2" and "a6"); macrocycle and C25 hydroxyl therein ("a5" vs. Lpm), β-D-rhamnosyl moiety and C6' methyl therein ("e1" vs. "d1" and "a7"; "a6" vs. Lpm), and homodichloro-orsellinyl moiety and C8" methyl, C3" chlorine, and C5" chlorine therein ("d1" vs. Lpm; "a2"-"a4" vs. Lpm; "a8" vs. "a6"). The observation that the Lpm C4" hydroxyl is exposed to solvent at the exterior of RNAP (Fig. S3B-C) predicts that substituents--including very large substituents--may be introduced at the C4" hydroxyl oxygen without eliminating ability to inhibit RNAP, provided the H-bond-acceptor character of the oxygen is maintained. Validating this prediction, we have prepared a Lpm analog having a large substituent, benzyl, appended at the C4" hydroxyl oxygen by semi-synthesis from Lpm and have found the analog to retain high activity in inhibiting RNAP (Fig. S5, analog "a1"; potencies within approximately an order of magnitude of that of Lpm for *Mtb* and *S. aureus* RNAP and equal to that of Lpm for *Escherichia coli* RNAP).

Relationship between binding site and resistance determinant of Lpm and binding sites and resistant determinants of other RNAP inhibitors

The binding site on RNAP for Lpm (cyan in Fig. 2A) does not overlap the binding sites of other RNAP inhibitors, including rifampin and sorangicin (Rif and Sor; Campbell et al., 2001, 2005); GE23077 and pseudoridimycin (GE and PUM; Zhang et al., 2014; Maffioli et al., 2017), CBR703 and D-AAP-1 (CBR and AAP; Lin et al., 2017; Feng et al., 2015; Bae et al., 2015), salinamide (Sal; Degen et al., 2014), streptolydigin (Stl; Tuske et al., 2005; Temiakov et al., 2005), and myxopyronin, corallopyronin, ripostatin, and squaramide (Myx, Cor, Rip, and SQ; Mukhopadhyay et al., 2008; Belogurov et al., 2009;

Molodtsov et al., 2015) (Fig. 2A). The binding site for Lpm is close to, but does not overlap, the binding site of Myx, Cor, Rip and SQ, which bind to the RNAP switch region, contacting SW1 and the face of SW2 opposite the face contacted by Lpm. The binding site for Lpm is far from the binding sites of other RNAP inhibitors.

Amino acid substitutions conferring resistance to Lpm were identified by sequencing spontaneous *Bacillus subtilis* Lpm-resistant mutants (Sonenshein et al., 1977; Ebright, 2005); additional substitutions were identified by sequencing induced Lpm-resistant mutants of *E. coli* RNAP (Ebright, 2005); and, in this work, a full set of substitutions was identified by extending the latter method (Fig. 2B-C). Lpm-resistant substitutions are obtained at ten sites in RNAP β subunit and seven sites in RNAP β′ subunit (Fig. 2B-C). All sites of Lpm-resistant substitutions are located in the immediate vicinity of the Lpm binding site (Fig. 2B), and all high-level (≥4-fold) Lpm-resistant substitutions involve RNAP residues that make direct contact with Lpm or that contact other RNAP residues that, in turn, make direct contact with Lpm (Fig. S5A). The resistance determinant for Lpm does not overlap the resistance determinants of other RNAP inhibitors (Fig. 2B). Consistent with the absence of overlap of binding sites and resistance determinants, mutants resistant to Lpm are not cross-resistant to other RNAP inhibitors (Figs. 2D, S6B), and, reciprocally, mutants resistant to other RNAP inhibitors are not cross-resistant to Lpm (Figs. 2E, S6C). Further consistent with the absence of overlap of binding sites and resistance determinants, Lpm and Rif exhibit additive antibacterial activity when co-administered (Fig. 2F).

Effects of Lpm on RNAP clamp conformation: cryo-EM data

The RNAP clamp adopts different conformations--ranging from open, to partly closed, to closed--in different crystal structures (Landick, 2001; Cramer et al., 2001; Chakraborty et al., 2012; Fig. 3A). Differences in clamp conformation arise from rigid-body rotations about a hinge formed by the RNAP switch region (Landick, 2001; Cramer et al., 2001; Chakraborty et al., 2012). Importantly, differences in clamp conformation are observed even in crystal structures of RNAP from a single bacterial species,

indicating that differences in clamp conformations are state differences and not species differences (Fig. 3A; Table 2).

In the cryo-EM structure of *Mtb* RNAP-Lpm, the clamp adopts an open conformational state, superimposable on the open state in a crystal structure of *Thermus thermophilus* (*Tth*) RNAP (Table 2), but differing by 9° from the partly closed state in a crystal structure of *Tth* RNAP (PDB: 5TMC), and differing by 17° from the closed state in crystal structures of catalytically competent RNAP-promoter transcription initiation complexes (*Tth* RPo and *Mtb* RPo; 4G7H and 5UH5) (Fig. 3B-C). The interactions that Lpm makes with βa16α1, β′a4α1, SW2, SW3, and SW4 require an open clamp conformation (Fig. 3D). Each of these regions is positioned to accommodate Lpm in the open state, but not in partly closed and closed states. In particular, βa16α1 and β′a4α1 would severely clash with Lpm in partly closed and closed states (Fig. 3D). We infer that Lpm, through its interactions with its binding site, induces or stabilizes an open clamp conformation.

Effects of Lpm on RNAP clamp conformation: single-molecule FRET data

RNAP clamp conformation in solution can be monitored by single-molecule fluorescence resonance energy transfer (FRET) experiments assessing distances between fluorescent probes incorporated specifically at the tips of the two walls of the RNAP active-center cleft (Chakraborty et al., 2012; Fig. 4A-C). Single-molecule FRET experiments analyzing RNAP holoenzyme in the absence of Lpm show a broad multimodal distribution of FRET efficiencies, indicative of open, partly closed, and closed states (Fig. 4D, left panel, gray curve). In contrast, analogous experiments in the presence of Lpm show a narrow unimodal peak with a FRET efficiency indicative of the open state (Fig. 4E, left panel). We conclude that Lpm traps the open-clamp state in solution. Single-molecule time traces in the absence of Lpm show static and dynamic molecules; the dynamic molecules (34%; N = 207) show transitions between three distinct FRET efficiency levels--corresponding to open-clamp, partly-closed-clamp, and closed-clamp states, with dwell times on the 100-400 ms time scale--indicating dynamic transitions between interconverting clamp states (Fig. 4D, left panel, colored curves; Fig. 4D, right panel; Fig. 4F).

In contrast, analogous single-molecule time traces in the presence of Lpm show only the FRET efficiency level corresponding to the open-clamp state, indicating stable trapping of the open-clamp state (Fig. 4E, right panel; Fig 4F). Single-molecule time traces before and after addition of Lpm show a rapid (<2 s) transition from the multimodal, dynamic clamp profile of RNAP in the absence of Lpm to the unimodal, non-dynamic clamp profile of RNAP in the presence of Lpm, demonstrating rapid trapping of the open-clamp state (Fig. 4G). We conclude, based both on cryo-EM structure and on FRET, that Lpm traps the open-clamp state.

Strikingly, the effect of Lpm on RNAP clamp conformation is *opposite* the effects of Myx, Cor, and Rip on RNAP clamp conformation. Lpm, through interactions with RNAP switch-region SW2, SW3, and SW4, traps an open-clamp state (Chakraborty et al., 2012); in contrast, Myx, Cor and Rip, through interactions with SW1 and the opposite face of SW2, trap a closed-clamp state (Figs. 3-4). The different effects of these inhibitors on RNAP clamp conformation presumably underlie their different effects on isomerization of RPc to RPo [inhibition of an early step in isomerization by Lpm; inhibition of a later step in isomerization by Myx, Cor, and Rip (Tupin et al., 2010; Artsimovitch et al., 2012)].

The binding site on RNAP for Lpm overlaps the proposed binding site on RNAP for pause-inducing and termination-inducing RNA hairpins (Hein et al., 2014). It is attractive to speculate that the Lpm binding site is an "allosteric trigger" for RNAP clamp opening and that ligands of this site--including not only Lpm but also pause-inducing and termination-inducing RNA hairpins--trigger RNAP clamp opening by binding to the site.

Mechanism of transcription inhibition by Lpm

The effects of Lpm on RNAP clamp conformation suggest a model for the mechanism by which Lpm inhibits isomerization of RPc to RPo (Sonenshein and Alexander, 1979; Ebright, 2005; Tupin et al., 2010; Artsimovitch et al., 2012) in transcription initiation (Fig. 5). Because σR2 [the σ module that recognizes promoter -10 elements (Ruff et al., 2015; Zhang et al., 2012; Zuo and Steitz, 2015; Bae et al., 2015; Feng et al., 2016)] interacts with the RNAP clamp and σR4 [the σ module that recognizes promoter

-35 elements (Ruff et al., 2015; Zuo and Steitz, 2015; Bae et al., 2015; Feng et al., 2016)] interacts with the main mass of RNAP, differences in RNAP clamp conformation necessarily result in differences in the spatial relationship of σR2 and σR4 (Fig. 5, left panels). We propose that, in the closed-clamp state, σR2 and σR4 can engage simultaneously with promoter -10 and -35 elements during formation of RPo (Fig. 5A, middle and right panels), but, in the open-clamp state, σR2 and σR4 cannot engage simultaneously with promoter -10 and -35 elements (Fig. 5B, middle and right panels). In particular, we propose that the σR2 "Trp wedge," which intercalates into DNA and stacks on the non-template-strand nucleotide at promoter position -12, nucleating promoter unwinding in formation of RPo (Bae et al., 2015; Feng et al., 2016), can engage DNA only in the closed-clamp state, and that the σR2 "NT-11 pocket," which captures an unstacked non-template-strand nucleotide at promoter position -11, stabilizing promoter unwinding upon formation of RPo (Zhang et al., 2012; Zuo and Steitz, 2015; Bae et al., 2015; Feng et al., 2016), can engage DNA only in the closed-clamp state (Fig. 5, middle and right panels). We suggest that the inability of the open-clamp state to engage simultaneously with -10 and -35 elements occurs during late steps in formation of RPo, when interactions of DNA downstream of the -10 element with the RNAP-active-center cleft constrain the -10 element to be near the RNAP active-center cleft, in a position unreachable by σR2 in the (Fig. 5, right panels), and possibly also occurs during earlier steps in formation of RPo, if, as proposed in Vassylyev et al., 2002 and NandyMazumdar et al., 2016, interactions of DNA downstream of the -10 element with the opposite wall of the RNAP active-center cleft constrain the -10 element to be near the RNAP active-center cleft, in a position unreachable by σR2 in the open-clamp state (Fig. 5, middle panels). The proposal that Lpm inhibits transcription initiation by trapping an open-clamp state, thereby preventing simultaneous engagement of -10 and -35 elements, is consistent with recently proposed models for transcription initiation (Feklistov et al., 2017).

Prospect

The methods and results of this report provide a strategy to obtain structural information for any RNAP inhibitor, irrespective of species selectivity and effects on RNAP conformation. The use of cryo-EM to determine the structure of RNAP-Lpm overcame obstacles that had precluded structure determination by X-ray crystallography: (1) the species selectivity of Lpm (which only poorly inhibits *Thermus* RNAP; Fig. S1B) and (2) the trapping by Lpm of an RNAP open-clamp conformation (which is incompatible with known crystal lattices of non-*Thermus* bacterial RNAP).

The results of this report provide fundamental information on the binding site and mechanism of Lpm and provide insights for antibacterial drug development involving Lpm. The primary limitation of Lpm as an antibacterial drug is that Lpm has no systemic bioavailability and thus is ineffective against systemic infections, such as tuberculosis and S. aureus blood and lung infections (Srivastava et al., 2011; Lancaster and Matthews, 2012; Venugopal and Johnson, 2012). The chemical strategy and synthetic procedure demonstrated here for appending substituents at the Lpm C4" hydroxyl (Fig S5; "a1") provides a means to overcome this limitation. It should be possible to append substituents improving physical and pharmacokinetic properties, nanoparticle drug-delivery modules, or even other antibacterial-agent pharmacophores at the Lpm C4" hydroxyl while retaining RNAP-inhibitory activity.

ACKNOWLEDGEMENTS

This work was supported by a Rega Foundation award to K.D. and NIH grants GM041376, AI104660, and AI109713-01 to R.H.E. We thank W. Fenical, H. Irschik, R. Jansen, A. L. Sonenshein, and E. Steinbrecher for compounds; J. Mukhopadhyay, S. Rodrigue, and J. Swezey for strains and plasmids; APS at Argonne National Laboratory for beamline access; the Rutgers University cryo-EM facility and the National Resource for Automated Molecular Microscopy (supported by NIH grant GM103310 and Simons Foundation grant 349247) for cryo-EM access; and K. Callanan, B. Carragher, and C. Potter for discussion.

AUTHOR CONTRIBUTIONS

W.L. and A.M prepared RNAP derivatives. W.L., K.D., Y.L, R.Y., Z.Z., E.E., and D.T. performed structure determination. D. Degen, R.Y.E., E.S., M.G., A.S., S.M., and Y.J. assessed RNAP-inhibitory activities, antibacterial activities, resistance, and cross-resistance. A.M., D. Duchi, and A.K. assessed FRET. Y.W.E., S.D., H.Z., and C.Z. prepared RNAP inhibitors. R.H.E. designed the study, analyzed data, and wrote the paper.

DECLARATION OF INTERESTS

R.H.E. has patent filings on the Lpm target (US8206898 and US8697354). The other authors declare no competing interests.

REFERENCES

Adams, P., Afonine, P., Bunkóczi, G., Chen, V., Davis, I., Echols, N., Headd, J., Hung, L., Kapral, G., Grosse-Kunstleve, R., McCoy, A., Moriarty, N., Oeffner, R., Read, R., Richardson, D., Richardson, J., Terwilliger, T., and Zwart, P. (2010). PHENIX: a comprehensive Python-based system for macromolecular structure solution. Acta Cryst, D *66*, 213.

Arnone, A., Nasini, G., and Cavalleri, B. (1987). Structure elucidation of the macrocyclic antibiotic lipiarmycin. J. Chem. Soc. Perkin Trans. I *6*, 1353-1359.

Artsimovitch, I., Seddon, J., and Sears, P. (2012). Fidaxomicin is an inhibitor of the initiation of bacterial RNA synthesis. Clin. Infect. Dis. *55*, S127-S131.

Babakhani, F., Gomez, A., Robert, N., and Sears, P. (2011). Killing kinetics of fidaxomicin and its major metabolite, OP-1118, against Clostridium difficile. J. Med. Microbiol. *60*, 1213-1217.

Bae, B., Feklistov, A., Lass-Napiorkowska, A., Landick, R., and Darst, S. (2015). Structure of a bacterial RNA polymerase holoenzyme open promoter complex. eLife *4*, e08504.

Bae, B., Nayak, D., Ray, A., Mustaev, A., Landick, R., and Darst, S. (2015). CBR antimicrobials inhibit RNA polymerase via at least two bridge-helix cap-mediated effects on nucleotide addition. Proc. Natl. Acad. Sci. USA *112*, E4178-E4187.

Banerjee, R., Rudra, P., Prajapati, R., Sengupta, S., and Mukhopadhyay, J. (2014). Optimization of recombinant *Mycobacterium tuberculosis* RNA polymerase expression and purification. Tuberculosis *94*, 397-404.

Belogurov, G., Vassylyeva, M., Svetlov, V., Klyuyev, S., Grishin, N., Vassylyev, D., and Artsimovitch, I. (2007). Structural basis for converting a general transcription factor into an operon-specific virulence regulator. Mol. Biosyst. *26*, 117-129.

Belogurov, G., Vassylyeva, M., Sevostyanova, A., Appleman, J., Xiang, A., Lira, R., Webber, S., Klyuyev, S., Nudler, E., Artsimovitch, I., and Vassylyev, D. (2009). Transcription inactivation through local refolding of the RNA polymerase structure. Nature *45*, 332-335.

Boland, A., Chang, L., and Barford, D. (2017). The potential of cryo-electron microscopy for structure-based drug design. Essays Biochem. *61*, 543-560.

Campbell, E., Korzheva, N., Mustaev, A., Murakami, K., Nair, S., Goldfarb, A., and Darst, S. (2001). Structural mechanism for rifampicin inhibition of bacterial RNA polymerase. Cell *104*, 901-912.

Campbell, E., Pavlova, O., Zenkin, N., Leon, F., Irschik, H., Jansen, R., Severinov, K., and Darst, S. (2005). Structural, functional, and genetic analysis of sorangicin inhibition of bacterial RNA polymerase. EMBO J. *24*, 674-682.

Chakraborty, A., Wang, D., Ebright, Y., and Ebright, R. H. (2010). Azide-specific labeling of biomolecules by Staudinger-Bertozzi ligation: phosphine derivatives of fluorescent probes suitable for single-molecule fluorescence spectroscopy. Meths Enzymol. *472*, 19-30.

Chakraborty, A., Wang, D., Ebright, Y., Korlann, Y., Kortkhonjia, E., Kim, T., Chowdhury, S., Wigneshweraraj, S., Irschik, H., Jansen, R., Nixon, B. T., Knight, J., Weiss, S., and Ebright, R. (2012). Opening and closing of the bacterial RNA polymerase clamp. Science *337*, 591-595.

Chakraborty, A., Mazumder, A., Lin, M., Hasemeyer, A., Xu, Q., Wang, D., Ebright, Y., and Ebright, R. H. (2015). Site-specific incorporation of probes into RNA polymerase by unnatural-amino-acid mutagenesis and Staudinger-Bertozzi ligation. Meths. Mol. Biol. *1276*, 101-131.

Chin, J., Martin, A., King, D., Wang, L., and Schultz, P. (2002). Addition of a photocrosslinking amino acid to the genetic code of Escherichia coli. Proc. Natl. Acad. Sci. USA *99*, 11020-11024.

Ciciliato, I., Corti, E., Sarubbi, E., Stefanelli, S., Gastaldo, L., Montanini, N., Kurz, M., Losi, D., Marinelli, F., and Selva, E. (2004). Antibiotics GE23077, novel inhibitors of bacterial RNA polymerase I. taxonomy, isolation and characterization. J. Antibiot. *57*, 210-217.

Coronelli, C., White, R., Lancini, G., and Parenti, F. (1975). Lipiarmycin, a new antibiotic from Actinoplanes. II. Isolation, chemical, biological and biochemical characterization. J. Antibiot. *28*, 253-259.

Cramer, P., Bushnell, D., and Kornberg, R. (2001). Structural basis of transcription: RNA polymerase II at 2.8 angstrom resolution. Science *292*, 1863-1876.

Datsenko, K., and Wanner, B. (2000). One-step inactivation of chromosomal genes in Escherichia coli K-12 using PCR products. Proc. Natl. Acad. Sci. USA. *97*, 6640-6645.

Degen, D., Feng, Y., Zhang, Y., Ebright, K. Y., Ebright, Y. W., Gigliotti, M., Vahedian-Movahed, H., Mandal, S., Talaue, M., Connell, N., Arnold, E., Fenical, W., and Ebright, R. H. (2014). Transcription inhibition by the depsipeptide antibiotic salinamide A. eLife *3*, e02451.

de la Rosa-Trevín, J., Quintana, A., Del Cano, L., Zaldívar, A., Foche, I., Gutiérrez, J., Gómez-Blanco, J., Burguet-Castell, J., Cuenca-Alba, J., Abrishami, V., Vargas, J., Otón, J., Sharov, G., Vilas, J., Navas, J., Conesa, P., Kazemi, M., Marabini, R., Sorzano, C., and Carazo, J. (2016). Scipion: A software framework toward integration, reproducibility and validation in 3D electron microscopy. J. Struct. Biol. *195*, 93-99.

Duchi, D., Bauer, D., Fernandez, L., Evans, G., Robb, N., Hwang, L., Gryte, K., Tomescu, A., Zawadzki, P., Morichaud, Z., Brodolin, K., and Kapanidis, A. (2016). RNA polymerase pausing during initial transcription. Mol. Cell *63*, 939-950.

Duchi, D., Gryte, K., Robb, N., Morichaud, Z., Sheppard, C., Brodolin, K., Wigneshweraraj, S., and Kapanidis, A. (2017). Conformational heterogeneity and bubble dynamics in single bacterial transcription initiation complexes. Nucl. Acids Res., (in press).

Ebright, R. (2005). RNA exit channel--target and method for inhibition of bacterial RNA polymerase. WIPO Patent Application WO/2005/001034.

Ebright, R., and Ebright, Y. (2012). Antibacterial agents: high-potency myxopyronin derivatives. WIPO Patent Application WO/2012/037508.

Emsley, P., Lohkamp, B., Scott, W. G., and Cowtan, K. (2010). Features and development of Coot. Acta Cryst. D *66*, 486.

Feklistov, A., Bae, B., Hauver, J., Lass-Napiorkowska, A., Kalesse, M., Glaus, F., Altmann, H., Heyduk, T., Landick, R., and Darst, S. A. (2017). RNA polymerase motions during promoter melting. Science *356*, 863-866.

Feng, Y., Degen, D., Wang, X., Gigliotti, M., Liu, S., Zhang, Y., Das, D., Michalchuk, T., Ebright, Y., Talaue, M., Connell, N., and Ebright, R. H. (2015). Structural basis of transcription inhibition by CBR hydroxamidines and CBR pyrazoles. Structure *23*, 1470-1481.

Feng, Y., Zhang, Y., and Ebright, R. H. (2016). Structural basis of transcription activation. Science *352*, 1330-1333.

Fernandez-Leiro, R., and Scheres, S. (2017). A pipeline approach to single-particle processing in RELION. Acta Cryst. D *73*, 496-502.

Fralick, J., and Burns-Keliher, L. (1994). Additive effect of tolC and rfa mutations on the hydrophobic barrier of the outer membrane of Escherichia coli K-12. J. Bacteriol. *176*, 6404-6406.

Ha, T., Ting, A., Liang, J., Caldwell, W., Deniz, A., Chemla, D., Schultz, P., and Weiss, S. (1999). Single molecule fluorescence spectroscopy of enzyme conformational dynamics and cleavage mechanism. Proc. Natl. Acad. Sci. USA *96*, 893-898.

Hein, P., Kolb, K., Windgassen, T., Bellecourt, M., Darst, S., Mooney, R., and Landick, R. (2014). RNA polymerase pausing and nascent-RNA structure formation are linked through clamp-domain movement. Nature Struct. Mol. Biol. *21*, 794-802.

Henderson, R., Sali, A., Baker, M., Carragher, B., and Devkota, B. (2012). Outcome of the first electron microscopy validation task force meeting. Structure *20*, 2015-214.

Hochlowski, J., Jackson, M., Rasmussen, R., Buko, A., Clement, J., Whittern, D., and McAlpine, J. (1997). Production of brominated tiacumicin derivatives. J. Antibiot. *50*, 201-205.

Holden, S., Uphoff, S., Hohlbein, J., Yadin, D., Le Reste, L., Britton, O., and Kapanidis, A. (2010). Defining the limits of single-molecule FRET resolution in TIRF microscopy. Biophys. J. *99*, 3102-3111.

Hubin, E., Fay, A., Xu, C., Bean, J., Saecker, R., Glickman, M., Darst, S., and Campbell, E. (2017). Structure and function of the mycobacterial transcription initiation complex with the essential regulator RbpA. eLife, e22520.

Hudson, B., Quispe, J., Lara-González, S., Kim, Y., Berman, H., Arnold, E., Ebright, R., and Lawson, C. (2009). Three-dimensional EM structure of an intact activator-dependent transcription initiation complex. Proc. Natl. Acad. Sci. U S A *106*, 19830-19835.

Ihle, N., Guzei, I., and Rheingold, A. (2000). Tiacumicin B acetone solvate. CSD Communication *https://www.ccdc.cam.ac.uk/structures/Search?Ccdcid=114782*.

Jokerst, R., Weeks, J., Zehring, W., and Greenleaf, A. (1989). Analysis of the gene encoding the largest subunit of RNA polymerase II in *Drosophila*. Mol. Gen. Genet. *215*, 266-275.

Kapanidis, A., Lee, N., Laurence, T., Doose, S., Margeat, E., and Weiss, S. (2004). Fluorescence-aided molecule sorting: Analysis of structure and interactions by alternating-laser excitation of single molecules. Proc. Natl. Acad. Sci. USA *101*, 8936-8941.

Kaufmann, E., Hattori, H., Miyatake-Ondozabal, H., and Gademann, K. (2015). Total synthesis of the glycosylated macrolide antibiotic fidaxomicin. Org. Lett. *17*, 3514-3517.

Kimanius, D., Forsberg, B., Scheres, S., and Lindahl, E. (2016). Accelerated cryo-EM structure determination with parallelisation using GPUs in RELION-2. Elife *5*, e18722.

Kucukelbir, A., Sigworth, F., and Tagare, H. (2014). Quantifying the local resolution of cryo-EM density maps. Nature Meths. *11*, 63-65.

Kurabachew, M., Lu, S., Krastel, P., Schmitt, E., Suresh, B., Goh, A., Knox, J., Ma, N., Jiricek, J., Beer, D., Cynamon, M., Petersen, F., Dartois, V., Keller, T., Dick, T., and Sambandamurthy, V. (2008). Lipiarmycin targets RNA polymerase and has good activity against multidrug-resistant strains of *Mycobacterium tuberculosis*. J. Antimicrob. Chemother. *62*, 713-719.

Lancaster, J., and Matthews, S. (2012). Fidaxomicin: the newest addition to the armamentarium against Clostridium difficile infections. Clin. Ther. *34*, 1-13.

Landick, R. (2001). RNA polymerase clamps down. Cell *105*, 567-570.

Lane, W., and Darst, S. (2010). Molecular evolution of multisubunit RNA polymerases: structural analysis. J. Mol. Biol. *395*, 686-704.

Lee, N., Kapanidis, A., Wang, Y., Michalet, X., Mukhopadhyay, J., Ebright, R., and Weiss, S. (2005). Accurate FRET measurements within single diffusing biomolecules using alternating-laser excitation. Biophys. J. *88*, 2939-2953.

Lin, W., Mandal, S., Degen, D., Liu, Y., Ebright, Y. W., Li, S., Feng, Y., Zhang, Y., Mandal, S., Jiang, Y., Liu, S., Gigliotti, M., Talaue, M., Connell, N., Das, K., Arnold, E., and Ebright, R. H. (2017). Structural basis of Mycobacterium tuberculosis transcription and transcription inhibition. Mol Cell *66*, 169-179.

Maffioli, S., Zhang, Y., Degen, D., Carzaniga, T., Del Gatto, G., Serina, S., Monciardini, P., Mazzetti, C., Guglierame, P., Candiani, G., Chiriac, A. I., Facchetti, G., Kaltofen, P., Sahl, H.-G., Dehò, G., Donadio, S., and Ebright, R. H. (2017). Antibacterial nucleoside-analog inhibitor of bacterial RNA polymerase: pseudouridimycin. Cell *169*, 1240-1248.

Meletiadis, J., Pournaras, S., Roilides, E., and Walsh, T. J. (2010). Defining fractional inhibitory concentration index cutoffs for additive interactions based on self-drug additive combinations, Monte Carlo simulation analysis, and in vitro-in vivo correlation data for antifungal drug combinations against *Aspergillus fumigatus*. Antimicrob. Agents Chemother. *54*, 602-609.

Merino, F., and Raunser, S. (2017). Electron cryo-microscopy as a tool for structure-based drug development. Angew. Chem. Int. Ed. Engl. *56*, 2846-2860.

Molodtsov, V., Fleming, P., Eyermann, C., Ferguson, A., Foulk, M., McKinney, D., Masse, C., Buurman, E., and Murakami, K. (2015). X-ray crystal structures of *Escherichia coli* RNA polymerase with switch region binding inhibitors enable rational design of squaramides with an improved fraction unbound to human plasma protein. J. Med. Chem. *58*, 3156-3171.

Mukhopadhyay, J., Das, K., Ismail, S., Koppstein, D., Jang, M., Hudson, B., Sarafianos, S., Tuske, S., Patel, J., Jansen, R., Irschik, H., Arnold, E., and Ebright, R. (2008). The RNA polymerase "switch region" is a target for inhibitors. Cell *135*, 295-307.

Murakami, K. (2013). The x-ray crystal structure of RNA polymerase σ^{70} holoenzyme. J. Biol. Chem. *288*, 9126-9134.

NandyMazumdar, M., Nedialkov, Y., Svetlov, D., Sevostyanova, A., Belogurov, G., and Artsimovitch, I. (2016). RNA polymerase gate loop guides the nontemplate DNA strand in transcription complexes. Proc. Natl. Acad. Sci. USA *113*, 14994-14999.

Niu, W., Kim, Y., Tau, G., Heyduk, T., and Ebright, R. (1996). Transcription activation at Class II CAP-dependent promoters: two interactions between CAP and RNA polymerase. Cell *87*, 1123-1134.

Niu, S., Hu, T., Li, S., Xiao, Y., Ma, L., Zhang, G., Zhang, H., Yang, X., Ju, J., and Zhang, C. (2011). Characterization of a sugar-O-methyltransferase TiaS5 affords new tiacumicin analogues with improved antibacterial properties and reveals substrate promiscuity. ChemBioChem, *12*, 1740-1748.

Otwinowski, Z., and Minor, W. (1997). Processing of X-ray diffraction data collected in oscillation mode. Meths. Enzymol. *276*, 307-326.

Paton, J., Holt, A., and Bywater, M. (1990). Measurement of MICs of antibacterial agents by spiral gradient endpoint compared with conventional dilution methods. Intl. J. Exp. Clin. Chemother. *3*, 31-38.

Rodrigue, S., Brodeur, J., Jacques, P., Gervais, A., Brzezinski, R., and Gaudreau, L. (2007). Identification of mycobacterial sigma factor binding sites by chromatin immunoprecipitation assays. J. Bacteriol. *189*, 1505-1513.

Sambrook, J., and Russell, D. (2001). Molecular Cloning: A Laboratory Manual (Cold Spring Harbor, NY, Cold Spring Harbor Laboratory).

Saxon, E., and Bertozzi, C. (2000). Cell surface engineering by a modified Staudinger reaction. Science *287*, 2007-2010.Ruff, E., Record, M., and Artsimovitch, I. (2015). Initial events in bacterial transcription initiation. Biomolecules *5*, 1035-1062.

Schalkowsky, S. (1994). Measures of susceptibility from a spiral gradient of drug concentrations. Adv. Exp. Med. Biol. *349*, 107-120.

Serra, S., Malpezzi, L., Bedeschi, A., Fuganti, C., and Fonte, P. (2017). Final demonstration of the co-identity of lipiarmycin A3 and tiacumicin B (fidaxomicin) through single crystal X-ray analysis. Antibiotics *6*.

Severinov, K., Mooney, R., Darst, S. A., and Landick, R. (1997). Tethering of the large subunits of Escherichia coli RNA polymerase. J. Biol. Chem. *272*, 24137-24140.

Sonenshein, A., and Alexander, H. (1979). Initiation of transcription in vitro inhibited by lipiarmycin. J. Mol. Biol. *127*, 55-72.

Sonenshein, A., Alexander, H., Rothstein, D., and S., F. (1977). Lipiarmycin-resistant ribonucleic acid polymerase mutants of *Bacillus subtilis*. J. Bacteriol. *132*, 73-79.

Srivastava, A., Talaue, M., Liu, S., Degen, D., Ebright, R. Y., Sineva, E., Chakraborty, A., Druzhinin, S., Chatterjee, S., Mukhopadhyay, J., Ebright, Y. W., Zozula, A., Shen, J., Sengupta, S., Niedfeldt, R., Xin, C., Kaneko, T., Irschik, H., Jansen, R., Donadio, S., Connell, N., and Ebright, R. H. (2011). New target for inhibition of bacterial RNA polymerase: "switch region." Curr. Opin. Microbiol. *14*, 532-543.

Suloway, C., Pulokas, J., Fellmann, D., Cheng, A., Guerra, F., Quispe, J., Stagg, S., Potter, C., and Carragher, B. (2005). Automated molecular microscopy: the new Leginon system. J. Struct. Biol. *151*, 41-60.

Sweetser, D., Nonet, M., and Young, R. (1987). Prokaryotic and eukaryotic RNA polymerases have homologous core subunits. Proc. Natl. Acad. Sci. USA *84*, 1192-1196.

Talpaert, M., Campagnari, F., and Clerici, L. (1975). Lipiarmycin: an antibiotic inhibiting nucleic acid polymerases. Biochem. Biophys. Res. Commun. *63*, 328-334.

Tang, H., Severinov, K., Goldfarb, A., Fenyo, D., Chait, B., and Ebright, R. (1994). Location, structure, and function of the target of a transcription activator protein. Genes Dev. *8*, 3058-3067.

Tang, H., Severinov, K., Goldfarb, A., and Ebright, R. H. (1995). Rapid RNA polymerase genetics: one-day, no-column preparation of reconstituted recombinant *Escherichia coli* RNA polymerase. Proc. Natl. Acad. Sci. USA *92*, 4902-4906.

Temiakov, D., Zenkin, N., Vassylyeva, M., Perederina, A., Tahirov, T., Kaihatsu, K., Savkina, M., Zorov, S., Nikiforov, V., Igarashi, N., Matsugaki, N., Wakatsuki, S., Severinov, K., and Vassylyev, D. (2005). Structural basis of transcription inhibition by antibiotic streptolydigin. Mol. Cell *19*, 655-666.

Theriault, R., Karwowski, J., Jackson, M., Girolami, R., Sunga, G., Vojtko, C., and Coen, L. (1987). Tiacumicins, a novel complex of 18-membered macrolide antibiotics. I. Taxonomy, fermentation and antibacterial activity. J. Antibiot. *40*, 567-574.

Tupin, A., Gualtieri, M., Leonetti, J., and Brodolin, K. (2010). The transcription inhibitor lipiarmycin blocks DNA fitting into the RNA polymerase catalytic site. EMBO J. *29*, 2527-2537.

Tuske, S., Sarafianos, S., Wang, X., Hudson, B., Sineva, E., Mukhopadhyay, J., Birktoft, J., Leroy, O., Ismail, S., Clark, A., Dharia, C., Napoli, A., Laptenko, O., Lee, J., Borukhov, S., Ebright, R., and Arnold, E. (2005). Inhibition of bacterial RNA polymerase by streptolydigin: stabilization of a straight-bridge-helix active-center conformation. Cell *122*, 541-552.

Vagin, A., and Teplyakov, A. (1997). MOLREP: An automated program for molecular replacement. J. Appl. Cryst. *30*, 1022-1025.

van de Meent, J., Bronson, J., Wiggins, C., and Gonzalez, R. (2014). Empirical Bayes methods enable advanced population-level analyses of single-molecule FRET experiments. Biophys. J. *106*, 1327-1337.

Vassylyev, D., Sekine, S., Laptenko, O., Lee, J., Vassylyeva, M., Borukhov, S., and Yokoyama, S. (2002). Crystal structure of a bacterial RNA polymerase holoenzyme at 2.6 Å resolution. Nature *417*, 712-719.

Venugopal, A., and Johnson, S. (2012). Fidaxomicin: a novel macrocyclic antibiotic approved for treatment of Clostridium difficile. Clin. Infect Dis. *54*, 568-574.

Wallace, A., and Corkill, J. (1989). Application of the spiral plating method to study antimicrobial actio. J. Microbiol. Meths. *10*, 303-310.

Wang, D., Meier, T., Chan, C., Feng, G., Lee, D., and Landick, R. (1995). Discontinuous movements of DNA and RNA in RNA polymerase accompany formation of a paused transcription complex. Cell *81*, 341-350.

Weixlbaumer, A., Leon, K., Landick, R., and Darst, S. (2013). Structural basis of transcriptional pausing in bacteria. Cell *152*, 431-441.

White, R., Burgess, D., Manduru, M., and Bosso, J. (1996). Comparison of three different in vitro methods of detecting synergy: time-kill, checkerboard, and E test. Antimicrob. Agents Chemother. *40*, 1914-1918.

Wu, P., and Brand, L. (1992). Orientation factor in steady-state and time-resolved resonance energy transfer measurements. Biochem. *31*, 7939-7947.

Xiao, Y., Li, S., Niu, S., Ma, L., Zhang, G., Zhang, H., Zhang, G., Ju, J., and Zhang, C. (2011). Characterization of tiacumicin B biosynthetic gene cluster affording diversified tiacumicin analogues and revealing a tailoring dihalogenase. J. Am. Chem. Soc. *133*, 1092-1105.

Zhang, G., Campbell, E., Minakhin, L., Richter, C., Severinov, K., and Darst, S. (1999). Crystal structure of *Thermus aquaticus* core RNA polymerase at 3.3 Å resolution. Cell *98*, 811-824.

Zhang, Y., Degen, D., Ho, M., Sineva, E., Ebright, K., Ebright, Y., Mekler, V., Vahedian-Movahed, H., Feng, Y., Yin, R., Tuske, S., Irschik, H., Jansen, R., Maffioli, S., Donadio, S., Arnold, E., and Ebright, R. H. (2014). GE23077 binds to the RNA polymerase 'i' and 'i+1' sites and prevents the binding of initiating nucleotides. eLife *3*, e02450.

Zhang, Y., Feng, Y., Chatterjee, S., Tuske, S., Ho, M., Arnold, E., and Ebright, R. H. (2012). Structural basis of transcription initiation. Science *338*, 1076-1080.

Zhang, K. (2016). Gctf: Real-time CTF determination and correction. J. Struct. Biol. *193*, 1-12.

Zheng, S., Palovcak, E., Armache, J., Verba, K., Cheng, Y., and Agard, D. (2017). MotionCor2: anisotropic correction of beam-induced motion for improved cryo-electron microscopy. Nature Meths. *14*, 331-333.

Zuo, Y., and Steitz, T. (2015). Crystal structures of the *E. coli* transcription initiation complexes with a complete bubble. Mol. Cell *58*, 534-540.

FIGURE LEGENDS

Figure 1. Structure of *Mtb* RNAP-Lpm

A, Density map for *Mtb* RNAP-Lpm (left) and Lpm (right), colored by local resolution. **B**, Density and atomic model for *Mtb* RNAP-Lpm. Gray, RNAP core other than β′*Mtb*SI; green, β′*Mtb*SI; yellow, σ; green mesh, density map for Lpm; cyan, Lpm; violet sphere, RNAP active-center Mg^{2+}. **C**, Atomic model for *Mtb* RNAP-Lpm. Colors as in **B**. **D**, RNAP-Lpm interactions (residues numbered as in *Mtb* RNAP and, in parentheses, as in *Escherichia coli* RNAP). Gray ribbons, RNAP backbone; gray sticks, RNAP carbon atoms; cyan sticks, Lpm carbon atoms; red, blue, and green sticks, oxygen, nitrogen, and chlorine atoms; dashed lines, H-bonds. **E**, Summary of RNAP-Lpm interactions. Blue arcs, van der Waals interactions; red dashed lines, H-bonds. See also Figs. S1-S4.

Figure 2. Relationship between binding site and resistance determinant of Lpm and binding sites and resistant determinants of other RNAP inhibitors

A, Binding positions of Lpm (cyan; Fig. 1), Rif and Sor (red; PDB: 1I6V, PDB: 1YNJ, PDB: 2A68, PDB: 2A69, PDB: 4KN4, PDB: 4KN7, PDB: 4OIR, and PDB: 5UHB), GE and PUM (dark blue; PDB: 4OIN, PDB: 4OIR, and PDB: 5X21), CBR and AAP (light blue; PDB: 4XSY, PDB: 4XSZ, PDB: 4ZH2, PDB: PDB: 4ZH3, PDB: 4ZH4, PDB: 5UHE, and PDB: 5UHF), Sal (green; PDB: 4MEX), Stl (yellow; PDB: 1ZYR), and Myx and SQ (magenta; PDB: 3DXJ, PDB: 3EQL, PDB: 4YFK, PDB: 4YFN, and PDB: 4YFX), mapped onto structure of *Mtb* RNAP (gray; two orthogonal views; β′*Mtb*SI and σ omitted for clarity). Violet sphere, RNAP active-center Mg^{2+}. **B**, Resistance determinants of Lpm (cyan; Fig. 2C), Rif and Sor (red; Campbell et al., 2001, 2005), GE and PUM (dark blue; Zhang et al., 2014; Maffioli et al., 2017), CBR703 and AAP (light blue; Lin et al., 2017; Feng et al., 2015; Bae et al., 2015), Sal (green; Degen et al., 2014), Stl (yellow; Tuske et al., 2005; Temiakov et al., 2005), and Myx, Cor, Rip, and SQ (magenta; Mukhopadhyay et al., 2008; Belogurov et al., 2009; Molodtsov et al., 2015) mapped onto structure of *Mtb* RNAP. **C**, Sequences and properties of *E. coli* Lpm-resistant mutants residues numbered

as in *Mtb* RNAP and, in parentheses, as in *Escherichia coli* RNAP). **D**, Absence of significant cross-resistance of *E. coli* Lpm-resistant mutants to Rif, GE, PUM, Sal, CBR, Stl, and Myx. **E**, Absence of significant cross-resistance of *E. coli* Rif-, GE/PUM-, Sal-, CBR-, and Stl-resistant mutants to Lpm. **F**, Additive antibacterial activity of Lpm and Rif. [Resistance and cross-resistance levels for Lpm-, CBR-, and Stl-resistant mutants are from strains having the mutant RNAP subunit gene on a plasmid and the corresponding wild-type RNAP subunit gene on the chromosome (merodiploid strains; see Methods). Resistance and cross-resistance levels for Lpm-, CBR-, and Stl-resistant mutants are from strains having the mutant RNAP subunit gene on the chromosome and no corresponding wild-type RNAP subunit gene (non-merodipoid strains; see Methods). Resistance and cross-resistance levels are expected to be lower for merodiploid strains than for non-merodiploid strains.] See also Fig. S5.

Figure 3. Effects of Lpm on RNAP clamp conformation: cryo-EM data

A, RNAP open (red), partly closed (yellow), and closed (green) clamp conformational states. *Mtb* RNAP-Lpm main mass (view as in Figs. 1-2) and, superimposed, RNAP clamps from crystal structures of *T. thermophilus* RNAP in different crystal lattices [*T. thermophilus* RNAP with open clamp (red; structure determined in this work to enable comparison of open-clamp, partly-closed-clamp, and closed-clamp states of RNAP from a single bacterial species; Table 2), *T. thermophilus* RNAP with partly open clamp (yellow; PDB: 5TMC), and *T. thermophilus* RPo (green; PDB: 4G7H)]. **B**, RNAP open-clamp state in *Mtb* RNAP-Lpm. Red, clamp in *Mtb* RNAP-Lpm. Other colors as in **A**. **C**, Comparisons of RNAP clamp conformation in *Mtb* RNAP-Lpm to RNAP clamp conformations in crystal structures of *Tth* RNAP with open clamp (left; Table 2), *Tth* RNAP with partly closed clamp (center; PDB: 5TMC), and *Tth* RPo with closed clamp (right; PDB: 4G7H). Each image shows *Mtb* RNAP-Lpm (clamp in red; view orientation and other colors as in Figs. 1-2) and, superimposed, the RNAP clamp of the comparator structure (gray). **D**, Stereodiagram of Lpm binding site showing conformations of RNAP structural elements SW1, SW2, SW3, SW4, βa16α1, and β'a4α1, in open-clamp (red; *Mtb* RNAP-Lpm), partly-closed clamp (yellow; PDB: 5TMC), and closed-clamp (green; PDB: 4G7H) states. RNAP

switches. SW1, SW2, SW3, and SW4 are shown with ends that connect to the RNAP clamp as numbered circles, and ends that connect to the RNAP main mass as numbered squares. Cyan, Lpm.

Figure 4. Effects of Lpm on RNAP clamp conformation: single-molecule FRET data

A, Use of unnatural-amino-acid mutagenesis, Staudinger ligation with Cy3B-phosphine and Alexa647-phosphine, and total-internal-reflection fluorescence microscopy with alternating-laser excitation microscopy (TIRF-ALEX) to obtain FRET data for single molecules of RNAP having fluorescent probes at the tips of the walls of the RNAP active-center cleft (see STAR Methods). Green, fluorescence donor probe Cy3B; red, fluorescent acceptor probe Alexa647; black square, hexahistidine tag. **B**, Surface-immobilization of fluorescent-probe-labelled RNAP for TIRF-ALEX. **C**, Time trace of donor emission intensity (green) and acceptor emission intensity (red) (top) and corresponding time trace of donor-acceptor FRET efficiency (bottom). **D**, Single-molecule FRET data for RNAP holoenzyme in absence of Lpm. Left, histogram. Gray, all states; colors, Hidden Markov Model (HMM)-assigned open, partly closed, and closed states (red, yellow, and green). Right, time trace with HMM-assigned open, partly closed, and closed states (red, yellow, and green). **E**, Single-molecule FRET data for RNAP holoenzyme in presence of Lpm (histogram and time trace as in **D**). **F**, Summary of RNAP clamp angles and dwell times for open, partly closed, and closed clamp states in absence and presence of Lpm. **G**, Time trace for RNAP holoenzyme before and after addition of Lpm.

Figure 5. Mechanism of transcription inhibition by Lpm

A, RNAP holoenzyme (left), RPc (center; DNA as in Ruff et al., 2015), and RPo (right, DNA as in Zuo and Steitz, 2015; Bae et al., 2015; Feng et al., 2016) for RNAP in absence of Lpm (closed clamp). σR2 and σR4 simultaneously engage promoter -10 and -35 elements in RPc and RPo. Atomic coordinates from PDB: 5UH5. Green ribbons, σ; green surface, σR2 NT-11 pocket; yellow surfaces, σR2 Trp wedge and σR4 recognition helix; blue, DNA. Other colors as in Figs. 1-2. **B**, As **A**, but for RNAP in presence of

Lpm (open clamp). σR2 and σR4 cannot simultaneously engage promoter -10 and -35 elements in RPc and RPo. Brown ribbons, σ; brown surface, σR2 NT-11 pocket; pink surface, σR2 Trp wedge and σR4 recognition helix; cyan, Lpm. Other colors as in **A**.

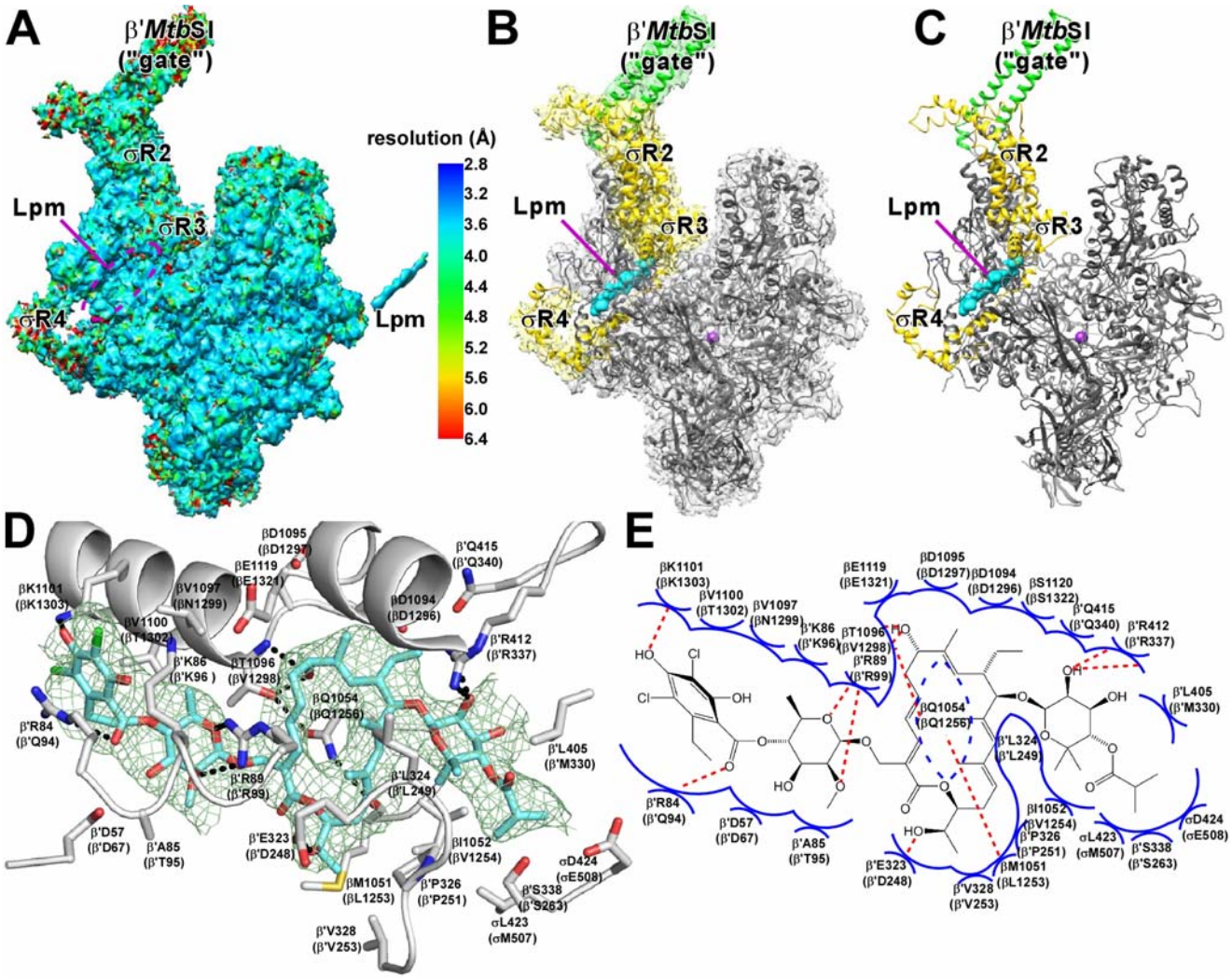
A
β'MtbSI ("gate")
σR2
Lpm
σR3
σR4
Lpm
resolution (Å)
2.8
3.2
3.6
4.0
4.4
4.8
5.2
5.6
6.0
6.4
B
β'MtbSI ("gate")
σR2
Lpm
σR3
σR4
C
β'MtbSI ("gate")
σR2
Lpm
σR3
σR4
D
βD1095 (βD1297)
βE1119 (βE1321)
β'Q415 (β'Q340)
βK1101 (βK1303)
βV1097 (βN1299)
βD1094 (βD1296)
βV1100 (βT1302)
β'R412 (β'R337)
β'K86 (β'K96)
βT1096 (βV1298)
βQ1054 (βQ1256)
β'R84 (β'Q94)
β'L405 (β'M330)
β'R89 (β'R99)
β'L324 (β'L249)
β'D57 (β'D67)
β'A85 (β'T95)
β'E323 (β'D248)
βI1052 (βV1254)
σD424 (σE508)
βM1051 (βL1253)
β'P326 (β'P251)
β'S338 (β'S263)
σL423 (σM507)
β'V328 (β'V253)
E
βK1101 (βK1303)
βE1119 (βE1321)
βD1095 (βD1297)
βD1094 (βD1296)
βS1120 (βS1322)
βV1100 (βT1302)
βV1097 (βN1299)
β'Q415 (β'Q340)
β'K86 (β'K96)
βT1096 (βV1298)
β'R412 (β'R337)
β'R89 (β'R99)
βQ1054 (βQ1256)
β'L405 (β'M330)
β'L324 (β'L249)
β'R84 (β'Q94)
β'D57 (β'D67)
βI1052 (βV1254)
β'P326 (β'P251)
σL423 (σM507)
σD424 (σE508)
β'A85 (β'T95)
β'S338 (β'S263)
β'E323 (β'D248)
βM1051 (βL1253)
β'V328 (β'V253)

Figure 1

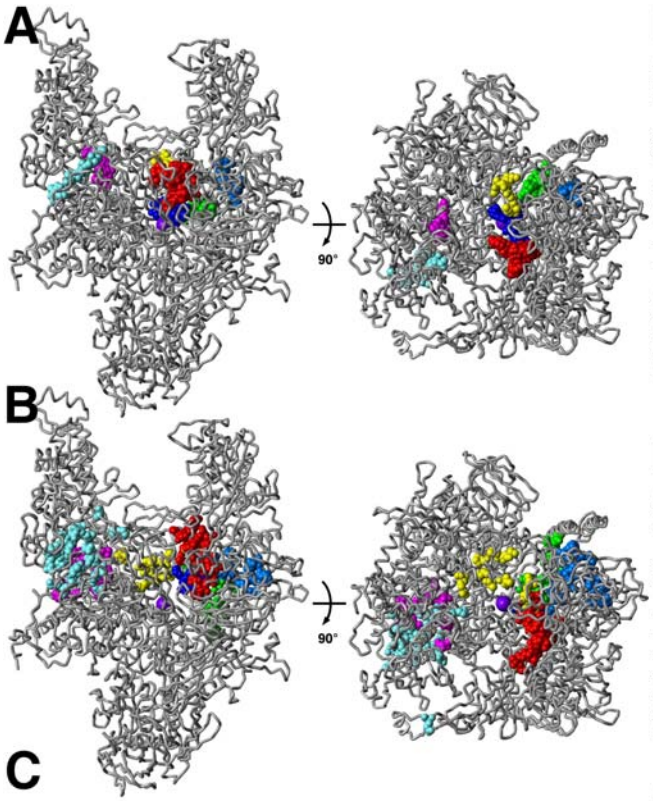

C

***E. coli* Lpm-resistant mutants: sequences and properties**

amino acid substitution	location	number of independent isolates	resistance level (MIC/MIC$_{wild\text{-}type}$)
***rpoB* (RNAP β subunit)**			
811 (892) Glu→Ala	---	1	2
1049 (1251) Tyr→Phe	switch 3	12	4
1054 (1256) Gln→Glu	switch 3	7	4
1054 (1256) Gln→Leu	switch 3	1	2
1086 (1288) Gln→Leu	---	1	2
1095 (1297) Asp→Ala	switch 4	5	4
1095 (1297) Asp→Tyr	switch 4	3	4
1100 (1302) Thr→Pro	---	1	2
1117 (1319) Met→Arg	β a16	10	8
1117 (1319) Met→Ile	β a16	7	2
1117 (1319) Met→Lys	β a16	6	8
1119 (1321) Glu→Val	β a16	5	4
1120 (1324) Asn→Lys	β a16	1	2
1123 (1325) Val→Ala	β a16	6	16
1123 (1325) Val→Glu	β a16	2	8
1123 (1325) Val→Gly	β a16	4	8
1123 (1325) Val→Leu	β a16	4	4
***rpoC* (RNAP β′ subunit)**			
86 (96) Lys→Ile	β′ a4	9	2
324 (249) Leu→Arg	β′ a8	6	4
338 (263) Ser→Thr	---	1	2
409 (334) Lys→Ile	switch 2	2	2
412 (337) Arg→His	switch 2	22	4
412 (337) Arg→Ser	switch 2	13	4
416 (341) Asn→Ser	switch 2	1	2
423 (348) Asp→Tyr	switch 2	4	4

D

***E. coli* Lpm-resistant mutants:**
absence of significant cross-resistance Rif, GE, PUM, Sal, CBR, Stl, and Myx

amino acid substitution	resistance level (MIC/MIC$_{wild\text{-}type}$)							
	Lpm	Rif	GE	PUM	Sal	CBR	Stl	Myx
***rpoB* (RNAP β subunit)**								
1049 (1251) Tyr→Phe	8	1	1	1	1	1	1	1
1054 (1256) Gln→Glu	8	1	1	1	1	1	1	2
1054 (1256) Gln→Leu	8	1	1	1	1	1	1	0.5
***rpoC* (RNAP β′ subunit)**								
412 (337) Arg→His	8	1	2	1	2	1	1	1
412 (337) Arg→Ser	8	1	2	1	2	1	2	1
423 (348) Asp→Tyr	8	2	1	1	1	1	1	1

E

***E. coli* Rif-resistant mutants:**
absence of significant cross-resistance to Lpm

amino acid substitution	cross-resistance level (MIC/MIC$_{wild\text{-}type}$)	
	Rif	Lpm
***rpoB* (RNAP β subunit)**		
441 (516) Asp→Val	512	0.5
451 (526) His→Asp	>1024	4
451 (526) His→Tyr	>1024	0.5
456 (531) Ser→Leu	1024	2

***E. coli* GE/PUM-resistant mutants:**
absence of significant cross-resistance to Lpm

amino acid substitution	cross-resistance level (MIC/MIC$_{wild\text{-}type}$)	
	GE	Lpm
***rpoB* (RNAP β subunit)**		
490 (565) Glu→Asp	>8	2
490 (565) Glu→Gly	>8	0.25
610 (684) Asn→Thr	16	2

***E. coli* Sal-resistant mutants:**
absence of significant cross-resistance to Lpm

amino acid substitution	cross-resistance level (MIC/MIC$_{wild\text{-}type}$)	
	Sal	Lpm
***rpoB* (RNAP β subunit)**		
601 (675) Asp→Ala	>256	0.5
603 (677) Asn→Lys	>256	1
***rpoC* (RNAP β′ subunit)**		
815 (738) Arg→Pro	128	1
856 (779) Ala→Val	256	2
859 (782) Gly→Ala	>256	1

***E. coli* CBR-resistant mutants:**
absence of significant cross-resistance to Lpm

amino acid substitution	cross-resistance level (MIC/MIC$_{wild\text{-}type}$)	
	CBR	Lpm
***rpoB* (RNAP β subunit)**		
477 (552) Pro→Met	4	1
543 (618) Gln→Leu	4	1
568 (642) Ser→Phe	4	1
580 (654) Asp→His	4	1
583 (657) Thr→Ile	4	1

***E. coli* Stl-resistant mutants:**
absence of significant cross-resistance to Lpm

amino acid substitution	cross-resistance level (MIC/MIC$_{wild\text{-}type}$)	
	Stl	Lpm
***rpoB* (RNAP β subunit)**		
468 (543) Ala→Val	64	1
470 (545) Phe→Cys	>64	1
***rpoC* (RNAP β′ subunit)**		
865 (788) Leu→Met	32	1
1029 (1139) Pro→Arg	8	1
1029 (1139) Pro→Leu	8	1

F

Additive antibacterial activity of Lpm and Rif

$FICI_{min}$	$FICI_{max}$	interaction type
0.91	2.2	additive

Figure 2

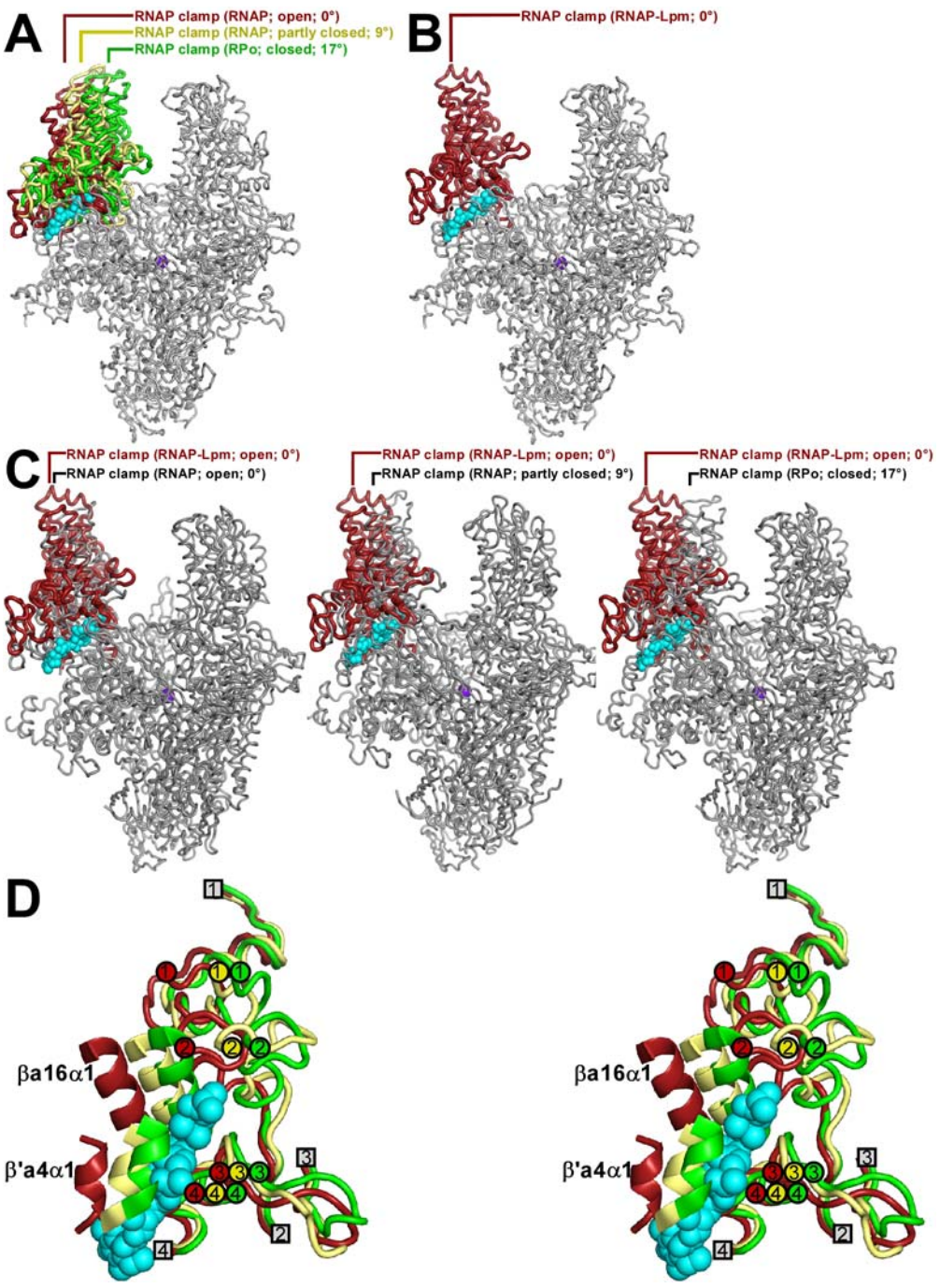
A
RNAP clamp (RNAP; open; 0°)
RNAP clamp (RNAP; partly closed; 9°)
RNAP clamp (RPo; closed; 17°)
B
RNAP clamp (RNAP-Lpm; 0°)
C
RNAP clamp (RNAP-Lpm; open; 0°)
RNAP clamp (RNAP; open; 0°)
RNAP clamp (RNAP-Lpm; open; 0°)
RNAP clamp (RNAP; partly closed; 9°)
RNAP clamp (RNAP-Lpm; open; 0°)
RNAP clamp (RPo; closed; 17°)
D
βa16α1
β'a4α1
βa16α1
β'a4α1

Figure 3

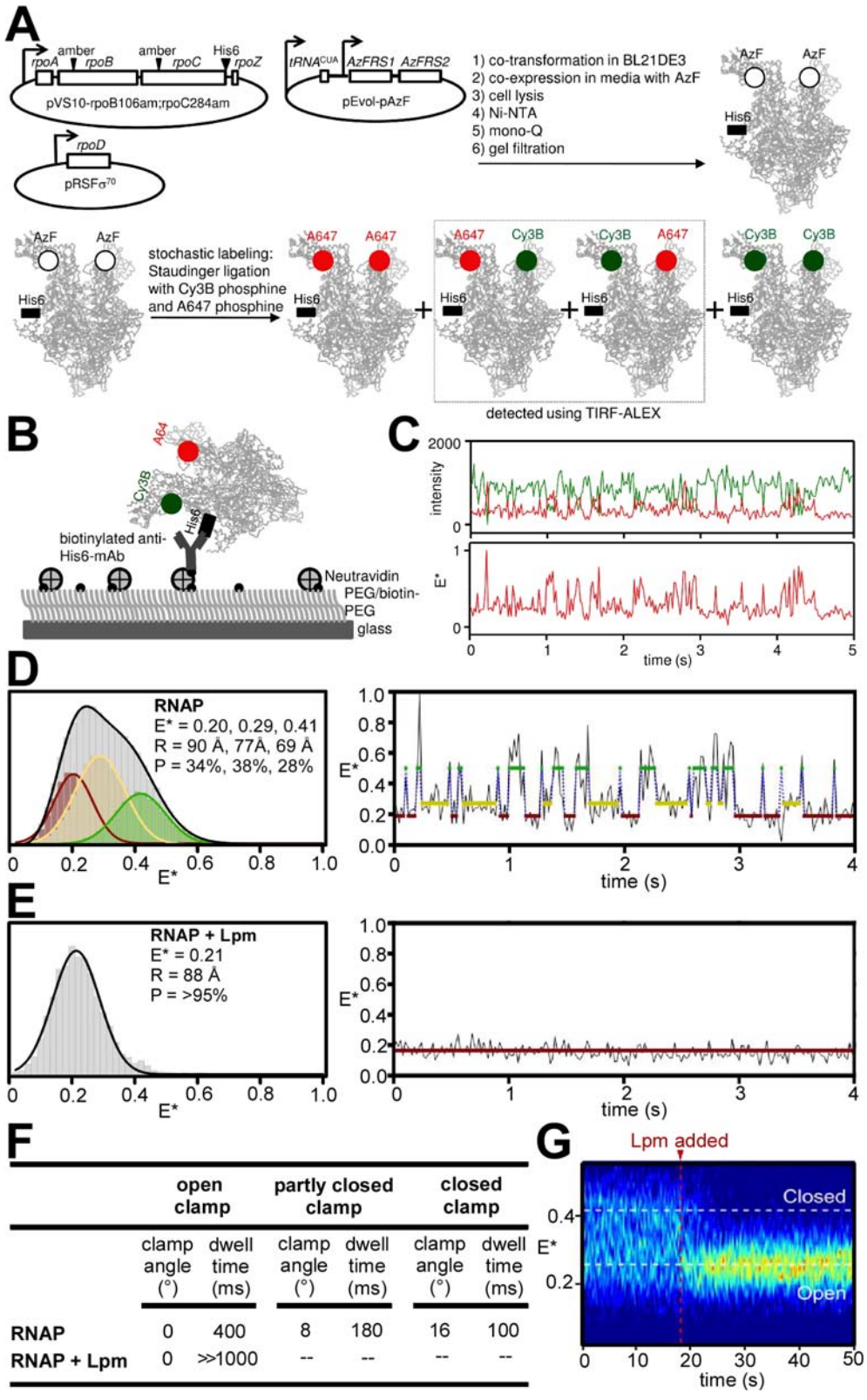

	open clamp		partly closed clamp		closed clamp	
	clamp angle (°)	dwell time (ms)	clamp angle (°)	dwell time (ms)	clamp angle (°)	dwell time (ms)
RNAP	0	400	8	180	16	100
RNAP + Lpm	0	>>1000	--	--	--	--

Figure 4

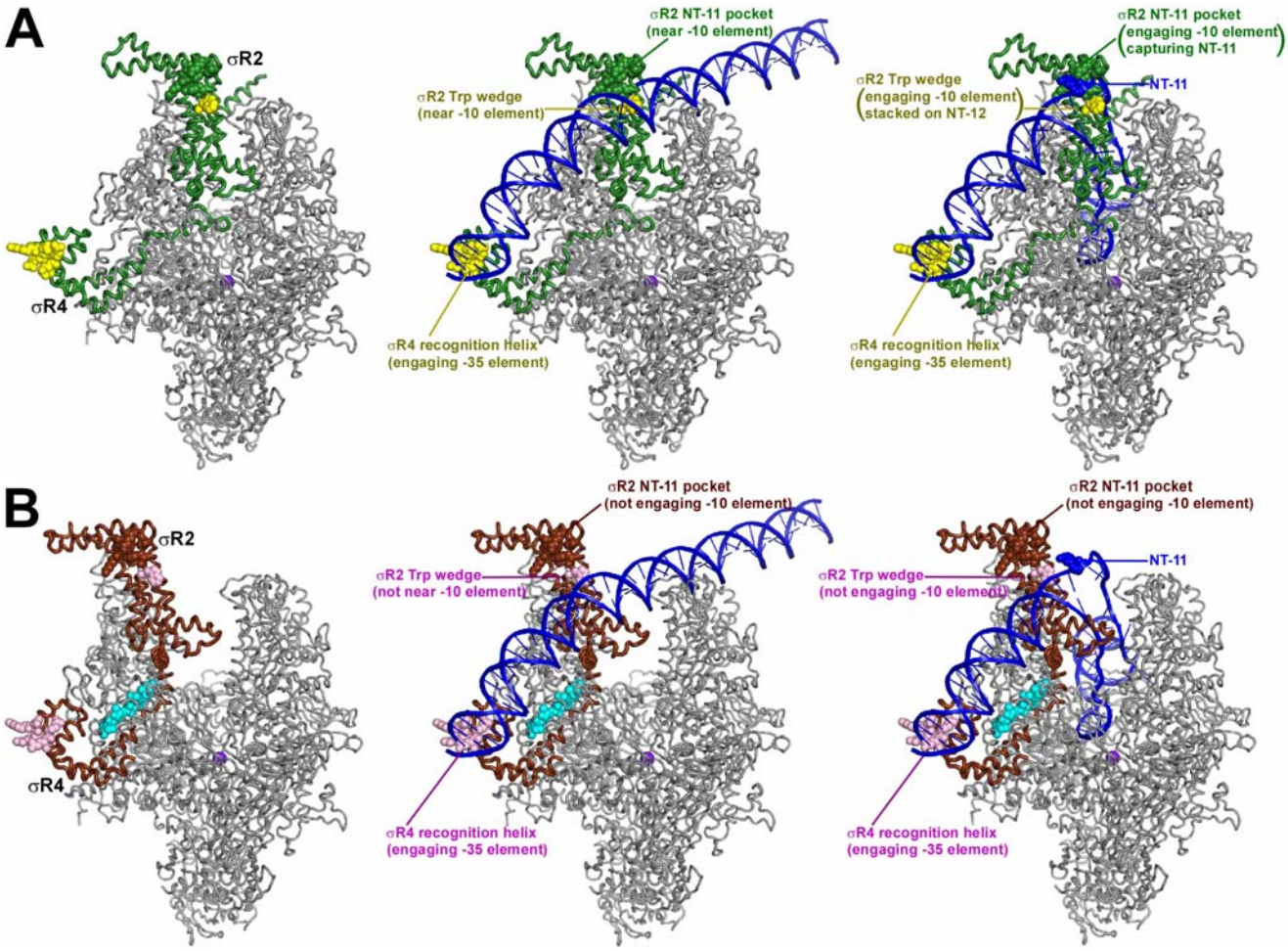
A
σR2
σR4
σR2 NT-11 pocket
(near -10 element)
σR2 Trp wedge
(near -10 element)
σR4 recognition helix
(engaging -35 element)
σR2 NT-11 pocket
(engaging -10 element
capturing NT-11
σR2 Trp wedge
(engaging -10 element
stacked on NT-12
NT-11
σR4 recognition helix
(engaging -35 element)
B
σR2
σR4
σR2 NT-11 pocket
(not engaging -10 element)
σR2 Trp wedge
(not near -10 element)
σR4 recognition helix
(engaging -35 element)
σR2 NT-11 pocket
(not engaging -10 element)
σR2 Trp wedge
(not engaging -10 element)
NT-11
σR4 recognition helix
(engaging -35 element)

Figure 5

Table 1. Cryo-EM data-collection and data-analysis statistics

structure	*Mtb* RNAP-Lpm	
EMDB and PDB codes	EMDB: 4230 PDB: 6FBV	
data collection		
number of grids used	2	
grid type	lacey carbon	
microscope/detector	Titan Krios/Gatan K2	
voltage (kV)	300 kV	
magnification	130,000x	
recording mode	counting mode	
dose rate (e-/s)	8	
pixel size (Å/pix)	1.061	
total dose (e-/Å^2)	72.05	
number of frames/movie	50	
total exposure time (s)	10	
defocus range (μm)	1.0 - 2.0	
data processing	**grid I**	**grid II**
number of micrographs	1,238	1,029
number of particles picked	452,912	366,594
number of particles after 2D/3D	126,977	97,412
combined dataset		
particles used for final map calculation	68,895	
map resolution (FSC 0.143; Å)	3.52	
map resolution (ResMap median; Å)	3.5	
structure/map fitting		
resolution (Å)	3.5	
map sharpening B factor (Å^2)	-109	
experimental map / model correlation	0.83	
experimental map / 2Fo-Fc correlation	0.98	
average B factor (Å^2)	95.3	
total number of atoms	25,156	
clash score	13	
Ramachandran plot		
favored (%)	94.5	
outliers (%)	0.03	
root-mean-square (RMS) deviations		
bond length (Å)	0.006	
bond angle (º)	1.027	

*Structure factors were from cryoEM map, and 2Fo-Fc map was from final model.

Table 2. X-ray crystallography data-collection and data-analysis statistics*

structure	*Tth* RNAP core
PDB code	PDB: 6ASG
data collection	
data collection source	APS-19ID
space group	R3
cell dimensions	
a, b, c (Å)	280.7,280.7,184.9
α, β, γ (°)	90.0, 90.0, 120.0
resolution	50.0-3.8 (4.0-3.8)
number of unique reflections	61,395
R_{merge}	0.245 (0.704)
R_{meas}	0.275 (0.830)
R_{pim}	0.124 (0.430)
highest resolution shell $CC_{1/2}$	0.418
I/σ(I)	5.0 (1.2)
completeness (%)	99.2 (92.3)
redundancy	4.8 (3.2)
refinement	
resolution (Å)	42.5-3.8
number of unique reflections	50,511
number of test reflections	2,611
R_{work}/R_{free}	0.22/0.27 (0.27/0.32)
number of atoms	
protein	23,551
ligand/ion	3
root-Mean-Square(RMS) Deviations	
bond length (Å)	0.003
bond angle (º)	0.658
MolProbity statistics	
clash score	15.2
rotamer outliers (%)	1.0
Cβ outliers (%)	0
Ramachandran plot	
Favored (%)	94.1
Outliers (%)	0.4

*Data for highest-resolution shells are in parentheses.

STAR*METHODS

REAGENT or RESOURCE	SOURCE	IDENTIFIER
Antibodies		
Penta-His Biotin Conjugate	QIAGEN	Cat# 34440
Bacterial and Virus Strains		
Escherichia coli BL21(DE3)	EMD Millipore	Cat# C600003
E.scherichia coli D21f2tolC (*rfa tolC*)	Fralick and Burns-Keliher, 1994	N/A
Escherichia coli D21f2tolC *rpoB-D516V*	Zhang et al., 2014	N/A
Escherichia coli D21f2tolC *rpoB-H526D*	Zhang et al., 2014	N/A
Escherichia coli D21f2tolC *rpoB-H526Y*	Zhang et al., 2014	N/A
Escherichia coli D21f2tolC *rpoB-S531L*	Zhang et al., 2014	N/A
Escherichia coli D21f2tolC *rpoB-E565D*	Maffioli et al., 2017	N/A
Escherichia coli D21f2tolC *rpoB-E565G*	Maffioli et al., 2017	N/A
Escherichia coli D21f2tolC *rpoB-D675A*	Degen et al., 2014	N/A
Escherichia coli D21f2tolC *rpoB-N677K*	Degen et al., 2014	N/A
Escherichia coli D21f2tolC *rpoB-N684T*	Zhang et al., 2014	N/A
Escherichia coli D21f2tolC *rpoB-Y1251F*	this paper	N/A
Escherichia coli D21f2tolC *rpoB-Q1256E*	Degen et al., 2014	N/A
Escherichia coli D21f2tolC *rpoB-Q1256L*	Degen et al., 2014	N/A
Escherichia coli D21f2tolC *rpoC-R337H*	Degen et al., 2014	N/A
Escherichia coli D21f2tolC *rpoC-R337S*	this paper	N/A
Escherichia coli D21f2tolC *rpoC-D348Y*	this paper	N/A
Escherichia coli D21f2tolC *rpoC-R738P*	Degen et al., 2014	N/A
Escherichia coli D21f2tolC *rpoC-A779V*	Degen et al., 2014	N/A
Escherichia coli D21f2tolC *rpoC-G782A*	Degen et al., 2014	N/A
Escherichia coli XE54	Tang et al., 1994	N/A
Escherichia coli XL1-Blue	Agilent / Stratagene	Cat# 200249
Dactylosporangium aurantiacum hamdenensis NRRL 18085	ARS Culture Collection	NRRL 18085
Thermus thermophilus HB-8	DSMZ	DSM 579
Chemicals, Peptides, and Recombinant Proteins		
lipiarmycin A3 (Lpm)	gift from A.L. Sonenschein	N/A
lipiarmycin A3 (Lpm)	this paper	N/A
lipiarmycin A3 (Lpm)	BioAustralis	Cat# BIA-F1356
lipiarmycin A3 (Lpm)	Biorbyt	Cat# orb146075
4"-O-benzyl-Lpm (Lpm analog "a1")	this paper	N/A
5"-deschloro-Lpm (Lpm analog "a2")	this paper	N/A
3",5"-dideschloro-Lpm (50-1d; Lpm analog "a3")	this paper	N/A
5"-bromo-3",5"-dideschloro Lpm (Lpm analog "a4")	this paper	N/A
69-1d (Lpm analog "a5")	Xiao et al., 2011 and Niu et al., 2011	N/A
70-9d (Lpm analog "a6")	Xiao et al., 2011 and Niu et al., 2011	N/A
70-10d (Lpm analog "a7")	Xiao et al., 2011 and Niu et al., 2011	N/A
70-11d (Lpm analog "a8")	Xiao et al., 2011 and Niu et al., 2011	N/A

OP-1118 (Lpm analog "b1")	Toronto Research Chemical	N/A
53-1d (Lpm analog "b2")	Xiao et al., 2011 and Niu et al., 2011	N/A
57-4d (Lpm analog "c1")	Xiao et al., 2011 and Niu et al., 2011	N/A
desaryl-Lpm (Lpm analog "d1")	this paper	N/A
54-3d (Lpm analog "e1")	Xiao et al., 2011 and Niu et al., 2011	N/A
rifampin (Rif)	Sigma-Aldrich	Cat# R3501
GE23077 (GE)	Ciciliato et al., 2004	N/A
pseudouridimycin (PUM)	Maffioli et al., 2017	N/A
salinamide A (Sal)	gift from W. Fenical	N/A
CBR703 (CBR)	Maybridge	Cat# RF05117SC
streptolydigin (Stl)	gift from E. Steinbrecher	N/A
myxopyronin B (Myx)	Ebright and Ebright, 2012	N/A
corallopyronin A (Cor)	gift from H. Irshick and R. Jansen	N/A
ripostatin A (Rip)	gift from H. Irshick and R. Jansen	N/A
Escherichia coli RNA polymerase (RNAP) σ^{70} holoenzyme	this paper	N/A
Alexa647, Cy3B-labelled *E coli* RNA polymerase (RNAP) σ^{70} holoenzyme	this paper	N/A
Mycobacterium tuberculosis RNA polymerase (RNAP) σ^{A} holoenzyme	Lin et al., 2017	N/A
Mycobacterium tuberculosis [Ala1101]β-RNA polymerase (RNAP) σ^{A} holoenzyme	this paper	N/A
Mycobacterium tuberculosis [Ala84]β′-RNA polymerase (RNAP) σ^{A} holoenzyme	this paper	N/A
Mycobacterium tuberculosis [Ala89]β′-RNA polymerase (RNAP) σ^{A} holoenzyme	this paper	N/A
Mycobacterium tuberculosis [Ala323]β′-RNA polymerase (RNAP) σ^{A} holoenzyme	this paper	N/A
Mycobacterium tuberculosis [Ala412]β′-RNA polymerase (RNAP) σ^{A} holoenzyme	this paper	N/A
Mycobacterium tuberculosis RNA polymerase (RNAP) core enzyme	Lin et al., 2017	N/A
Mycobacterium tuberculosis RNA polymerase (RNAP) core enzyme	Lin et al., 2017	N/A
Mycobacterium tuberculosis [Ala1101]β-RNA polymerase (RNAP) core enzyme	this paper	N/A
Mycobacterium tuberculosis [Ala84]β′-RNA polymerase (RNAP) core enzyme	this paper	N/A
Mycobacterium tuberculosis [Ala89]β′-RNA polymerase (RNAP) core enzyme	this paper	N/A
Mycobacterium tuberculosis [Ala323]β′-RNA polymerase (RNAP) core enzyme	this paper	N/A
Mycobacterium tuberculosis [Ala412]β′-RNA polymerase (RNAP) core enzyme	this paper	N/A
Mycobacterium tuberculosis σ^{A}	Lin et al., 2017	N/A
Staphylococcus aureus RNA polymerase (RNAP) σ^{A} holoenzyme	Maffioli et al., 2017	N/A
Thermus thermophilus RNA polymerase (RNAP) σ^{A} holoenzyme	Zhang et al., 2012	N/A
Thermus thermophilus RNA polymerase (RNAP) core enzyme	Zhang et al., 2012	N/A
HeLaScribe Nuclear Extract	Promega	Cat# E309A
γ-{2'-(2-benzothiazoyl)-60-hydroxybenzothiazole}-ATP	Jena Biosciences	Cat# NU-1700

fermentation growth media containing limiting chloride	Hochlowski et al., 1997	N/A
H-top-agar	Sambrook and Russell, 2001	N/A
LB broth	Sambrook and Russell, 2001	N/A
LB agar	Sambrook and Russell, 2001	N/A
ampicillin	Sigma-Aldrich	Cat# A0166
chloramphenicol	Sigma-Aldrich	Cat# C0378
kanamycin	Sigma-Aldrich	Cat# K4000
L-arabinose	Sigma-Aldrich	Cat# A3256
isopropyl-β-D-thiogalactoside (IPTG)	Gold Biotechnology	Cat# I2481C50
polyethyleneimine (Polymin P)	Sigma-Aldrich	Cat# P3143
4-azido-L-phenylalanine	Chem-Impex International	Cat# 06162
Alexa647-pentanoyl-ethylenediaminyl-phosphine	Chakraborty et al., 2010, 2015	N/A
Cy3B-carboyl-ethylenediaminyl-phosphine	Chakraborty et al., 2010, 2015	N/A
benzyl bromide	Sigma-Aldrich	Cat# B17905
n-octyl-β-D-glucopyranoside	Biosynth	Cat# O-2000
poly(acrylic acid sodium salt) 5,100 Da	Hampton Research	Cat# HR2-773
Vectabond aminosilane reagent	Vector Labs	Cat# SP-1800
methoxy-PEG succinimidyl valerate (mPEG-SVA)	Laysan Bio	Cat# MPEG-SVA-5000
biotinyl-PEG succinimidyl valerate (Biotin-PEG-SVA)	Laysan Bio	Cat# Biotin-PEG-SVA-5000
NeutrAvidin	ThermoFisher	Cat# 31000
Trolox	Sigma-Aldrich	Cat# 238813
glucose oxidase	Sigma-Aldrich	Cat# 345386
catalase	Sigma-Aldrich	Cat# C30
Critical Commercial Assays		
QuantiChromT Chloride Assay Kit	BioAssay Systems	Cat# DICL-250
HeLaScribe Nuclear Extract in vitro Transcription System	Promega	Cat# E3110
QuikChange site-directed mutagenesis kit	Agilent	Cat# 200519
QuikChange site-directed mutagenesis kit	Agilent	Cat# 200523
QuikChange site-directed mutagenesis kit	Agilent	Cat# 210518
Wizard Genomic DNA Purification Kit	Promega	Cat# A1125
Gel/PCR DNA Fragments Extraction Kit	IBI Scientific	Cat# IB47030
Wizard Classic 1 crystal screening solution kit	Emerald / Rigaku	Cat# 1009530
Wizard Classic 2 crystal screening solution kit	Emerald / Rigaku	Cat# 1009531
Wizard Classic 3 crystal screening solution kit	Emerald / Rigaku	Cat# 1009533
Wizard Classic 4 crystal screening solution kit	Emerald / Rigaku	Cat# 1009534
Wizard Cryo 1 crystal screening solution kit	Emerald / Rigaku	Cat# 1009536
Wizard Cryo 2 crystal screening solution kit	Emerald / Rigaku	Cat# 1009537
Crystal Screen Cryo crystal screening solution kit	Hampton Research	Cat# HR2-122
Crystal Screen 2 Cryo crystal screening solution kit	Hampton Research	Cat# HR2-121
Crystal Screen crystal screening solution kit	Hampton Research	Cat# HR2-110
Crystal Screen 2 crystal screening solution kit	Hampton Research	Cat# HR2-112
Detergent Screen HT crystal screening solution kit	Hampton Research	Cat# HR2-406
Additive Screen HT crystal screening solution kit	Hampton Research	Cat# HR2-138
Index crystal screening solution kit	Hampton Research	Cat# HR2-144
Natrix crystal screening solution kit	Hampton Research	Cat# HR2-116
Natrix 2 crystal screening solution kit	Hampton Research	Cat# HR2-117

PEG/Ion crystal screening solution kit	Hampton Research	Cat# HR2-126
PEG/Ion 2 crystal screening solution kit	Hampton Research	Cat# HR2-098
PEGRx 1 crystal screening solution kit	Hampton Research	Cat# HR2-082
PEGRx 2 crystal screening solution kit	Hampton Research	Cat# HR2-084
SaltRx 1 crystal screening solution kit	Hampton Research	Cat# HR2-107
SaltRx 2 crystal screening solution kit	Hampton Research	Cat# HR2-109
NeXtal Protein Complex Suite crystal screening solution kit	Qiagen	Cat# 130715
NeXtal Nucleix Suite crystal screening solution kit	Qiagen	Cat# 130719
Deposited Data		
Mycobacterium tuberculosis RNA polymerase σ^A holoenzyme in complex with lipiarmycin A3 (Lpm	this paper	EMDB: 4230 PDB: 6FBV
Thermus thermophilus RNA polymerase core enzyme	this paper	PDB: 6ASG
Recombinant DNA		
pCOLA-Duet-1	Novagen / EMD Millipore	Cat# 71406
pCOLADuet-Mtb-*rpoBC*	this paper	N/A
pCOLADuet-Mtb-*rpoB*-K1101A-*rpoC*	this paper	N/A
pCOLADuet-Mtb-*rpoB*-*rpoC*-R84A	this paper	N/A
pCOLADuet-Mtb-*rpoB*-*rpoC*-R89A	this paper	N/A
pCOLADuet-Mtb-*rpoB*-*rpoC*-E323A	this paper	N/A
pCOLADuet-Mtb-*rpoB*-*rpoC*-R412A	this paper	N/A
pEVOL-pAzF	Chin et al., 2002	N/A
pJF09	Rodrigue et al., 2007	N/A
pJF10	Rodrigue et al., 2007	N/A
pREII-NHα	Niu et al., 1996	N/A
pRL663	Wang et al., 1995	N/A
pRL663-K96I	this paper	N/A
pRL663-L249R	this paper	N/A
pRL663-S263T	this paper	N/A
pRL663-K334I	this paper	N/A
pRL663-R337H	this paper	N/A
pRL663-R337S	this paper	N/A
pRL663-N341S	this paper	N/A
pRL663-K345N	Mukhopadhyay et al., 2008	N/A
pRL663-K345Q	Mukhopadhyay et al., 2008	N/A
pRL663-K345R	Mukhopadhyay et al., 2008	N/A
pRL663-K345T	Mukhopadhyay et al., 2008	N/A
pRL663-D348Y	this paper	N/A
pRL663-L788M	Tuske et al., 2005	N/A
pRL663-P1139R	Tuske et al., 2005	N/A
pRL663-P1139L	Tuske et al., 2005	N/A
pRL663-G1346D	Mukhopadhyay et al., 2008	N/A
pRL663-V1351F	Mukhopadhyay et al., 2008	N/A
pRL663-I1352N	Mukhopadhyay et al., 2008	N/A
pRL663-I1352S	Mukhopadhyay et al., 2008	N/A
pRL663-G1354C	Mukhopadhyay et al., 2008	N/A
pRL706	Severinov et al., 1997	N/A
pRL706-A543V	Tuske et al., 2005	N/A

pRL706-F545C	Tuske et al., 2005	N/A
pRL706-P552M	Feng et al., 2015	N/A
pRL706-Q618L	Feng et al., 2015	N/A
pRL706-S642F	Feng et al., 2015	N/A
pRL706-D654H	Feng et al., 2015	N/A
pRL706-T657I	Feng et al., 2015	N/A
pRL706-E892A	this paper	N/A
pRL706-M1232I	Mukhopadhyay et al., 2008	N/A
pRL706-Y1251F	this paper	N/A
pRL706-T1255I	Mukhopadhyay et al., 2008	N/A
pRL706-Q1256E	this paper	N/A
pRL706-Q1256L	this paper	N/A
pRL706-V1275F	Mukhopadhyay et al., 2008	N/A
pRL706-V1275M	Mukhopadhyay et al., 2008	N/A
pRL706-L1278V	Mukhopadhyay et al., 2008	N/A
pRL706-E1279G	Mukhopadhyay et al., 2008	N/A
pRL706-E1279K	Mukhopadhyay et al., 2008	N/A
pRL706-A1283V	Mukhopadhyay et al., 2008	N/A
pRL706-Y1285D	Mukhopadhyay et al., 2008	N/A
pRL706-Q1288L	this paper	N/A
pRL706-L1291F	Mukhopadhyay et al., 2008	N/A
pRL706-D1297A	this paper	N/A
pRL706-D1297Y	this paper	N/A
pRL706-V1298L	Mukhopadhyay et al., 2008	N/A
pRL706-T1302P	this paper	N/A
pRL706-M1315L	Mukhopadhyay et al., 2008	N/A
pRL706-P1317L	Mukhopadhyay et al., 2008	N/A
pRL706-M1319I	this paper	N/A
pRL706-M1319K	this paper	N/A
pRL706-M1319R	this paper	N/A
pRL706-P1320A	Mukhopadhyay et al., 2008	N/A
pRL706-E1321V	this paper	N/A
pRL706-S1322P	Mukhopadhyay et al., 2008	N/A
pRL706-S1322T	Mukhopadhyay et al., 2008	N/A
pRL706-S1322V	Mukhopadhyay et al., 2008	N/A
pRL706-S1322Y	Mukhopadhyay et al., 2008	N/A
pRL706-N1324K	this paper	N/A
pRL706-V1325A	this paper	N/A
pRL706-V1325E	this paper	N/A
pRL706-V1325G	this paper	N/A
pRL706-V1325L	this paper	N/A
pRL706-L1326W	Mukhopadhyay et al., 2008	N/A
pRSFduet-sigma	Hudson et al., 2009	N/A
pVS10	Belogurov et al., 2007	N/A
pVS10-rpoB106am;rpoC284am	this paper	N/A
Software and Algorithms		

Coot	Emsley et al., 2010	https://www2.mrc-lmb.cam.ac.uk/personal/pemsley/coot/
ebFRET	van de Meent et al., 2014	http://ebfret.github.io/
FSC	Henderson et al., 2012	http://www.imagescience.de/fsc.html
Gctf	Zhang, 2016	https://www.mrc-lmb.cam.ac.uk/kzhang/Gctf/
HKL2000	Otwinowski and Minor, 1997	http://www.hkl-xray.com/
Leginon	Suloway et al., 2005	http://www.leginon.org
MotionCor2	Zheng et al., 2017	http://msg.ucsf.edu/em/software/motioncor2.html
Molrep	Vagin and Teplyakov, 1997	http://www.ccp4.ac.uk/html/molrep.html
MATLAB	Mathworks	https://www.mathworks.com/products/matlab.html
Origin	OriginLab	https://www.originlab.com/index.aspx?go=PRODUCTS/Origin
Phenix	Adams et al., 2010	https://www.phenix-online.org/
Relion v2.0.5	Fernandez-Leiro and Scheres, 2017	https://www2.mrc-lmb.cam.ac.uk/relion/index.php?title=Main_Page
ResMap	Kucukelbir et al., 2014	http://resmap.sourceforge.net/
Scipion v1.1	de la Rosa-Trevín et al., 2016	https://github.com/I2PC/scipion/wiki
SGE Spiral Gradient Endpoint v1.3	Spiral Biotech	N/A
SigmaPlot	Systat Software	https://systatsoftware.com/products/sigmaplot/
TwoTone-ALEX	Holden et al., 2010	https://groups.physics.ox.ac.uk/genemachines/group/Main.Software.html
Xmipp	Sorzano et al., 2004	http://xmipp.cnb.csic.es/twiki/bin/view/Xmipp/WebHome

Other		
Titan Krios 300 keV cryo-electron microscope	FEI / ThermoFisher	N/A
K2 Summit direct electron detection camera	Gatan	N/A
GIF Quantum imaging filter	Gatan	N/A
PELCO easiGlow glow discharge cleaning system	Ted Pella	N/A
EM GP grid plunger	Leica	N/A
Ubuntu 16.04 Linux GPU workstation	Titan Computers	N/A
GeForce GTX 1080 Ti graphics card	Nvidia	N/A
Gryphon liquid handling system	Art Robbins Instruments	N/A

Total-internal-reflection fluorescence (TIRF) microscope	Holden et al., 2010; Duchi et al., 2016, 2017	N/A
Samba 532 nm green laser	Cobolt	N/A
CUBE 635-30E red laser	Coherent	N/A
100x oil immersion objective (numerical aperture 1.4)	Olympus	N/A
1205C acousto-optical modulator	Isomet	N/A
Dichroic mirror (545 nm/650 nm)	Semrock	N/A
Dichroic mirror (630 nm DRLP)	Omega	N/A
545 nm LP emission filter	Chroma	Cat# HQ545LP
633/25 nm notch filter	Semrock	Cat#NF03-633E-25
iXon 897 EMCCD camera	Andor Technology	N/A
MS-2000 motorized x/y-scanning stage	ASI	N/A
Hitachi 2000 series HPLC system with L2455 detector	Hitachi	N/A
Hitachi 7000 series HPLC system with L7450 detector	Hitachi	N/A
ÄKTApurifier 10 FPLC system	GE Healthcare	Cat# 28406264
Luna C18 HPLC column (5 µm; 100 Å; 250 x 4.6 mm)	Phenomenex	Cat# 00G-4041-E0
Supelco Discovery BIO Wide Pore C18 semi-prep HPLC column (10 µm; 300 Å; 250 x 10 mm)	Sigma-Aldrich	Cat# 567209-U
HiLoad 16/60 Superdex 200 column	GE Healthcare	Cat# 17-1069-01
Mono Q 10/100 GL column	GE Healthcare	Cat# 17-5167-01
Silica gel, pore size 60 Å, 200-425 mesh particle size	Sigma-Aldrich	Cat# 236772
Ni-NTA agarose	Qiagen	Cat# 30230
Amicon Ultra-15 30K centrifugal filters	EMD Millipore	Cat# UFC903024
EmusliFlex-C5 cell disruptor	Avestin	N/A
Lambda 25 UV/Vis spectrophotometer	PerkinElmer	N/A
GENios Pro microplate reader	Tecan	N/A
GeneAmp 9700 PCR thermal cycler	Applied Biosystems	N/A
Autoplate 4000 spiral plater	Spiral Biotech	N/A
SGE transparent plastic template	Spiral Biotech	N/A
Lacey carbon film grids	Electron Microscopy Sciences	Cat#LC300-CU-100
Borosilicate glass coverslips #1.5	Menzel / ThermoFisher	Cat# 15654786
CultureWell 6 mm silicone gasket	Grace Bio-Labs	Cat# 103280
Whatman filter paper, Grade 1	Sigma-Aldrich	Cat# WHA1001150
Whatman filter paper, Grade 541	Sigma-Aldrich	Cat# WHA1541070

CONTACT FOR REAGENT AND RESOURCE SHARING

Requests for further information or reagents should be directed to Richard H. Ebright (ebright@waksman.rutgers.edu).

METHOD DETAILS

Lpm

Lpm was the kind gift of A.L. Sonenschein (Tufts University, Medford MA), was prepared as in Coronelli et al., 1975, or was purchased from BioAustralis or Biorbyt.

Lpm analogs: previously described Lpm analogs

Lpm analog "a4" (3"-bromo-3",5"-dideschloro-Lpm; compound 3 of Hochlowski et al., 1997) was prepared as in Hochlowski et al., 1997. Lpm analogs "a5" (69-1d), "a6" (70-9d), "a7" (70-10d), "a8" (70-11d), "b2" (53-11d), "c1" (54-4d), and "e1" (54-3d) were prepared as in Xiao et al., 2011 and Niu et al., 2011. Lpm analog "b1" (OP-1118; Babakhani et al., 2011) was purchased from Toronto Research Chemicals.

Lpm analogs: Lpm analogs "a2" (5"-deschloro-Lpm) and "d1" (desaryl-Lpm)

Lpm analogs "a2" (5"-deschloro-Lpm) and "d1" (desaryl-Lpm) were prepared by fermentation of the Lpm producer strain *Dactylosporangium aurantiacum* hamdenensis NRRL 18085 (Theriault et al., 1987; ARS Patent Culture Collection, Peoria IL) in growth media containing limiting chloride [growth media with KCl replaced by KBr; residual chloride concentration = 40 μM, quantified using QuantiChromT Chloride Assay Kit (BioAssays Systems)]. First-stage (0.2 L) and second-stage (10 L) cultures were prepared as in Hochlowski et al., 1997, and second-stage culture broths were harvested as in Hochlowski et al., 1997. Culture broths were adjusted to pH 7 by addition of 1 ml 12 N NaOH, supplemented with 5 L acetone, shaken 1 h at 22°C, and extracted with 3x4 L ethyl acetate. The extracts were evaporated, and the resulting material (20 g) was re-dissolved in 300 ml ethyl acetate, filtered through Whatman filter paper (Grade 1; Sigma-Aldrich), and evaporated. The resulting material (14 g) was partitioned in 900 ml 1:1:1 (v/v/v) chloroform-methanol-water, and the lower phase was evaporated. The resulting material

(11 g) was chromatographed on silica gel (Sigma-Aldrich; 3 cm x 30 cm; stepwise elution with 2-50% methanol in chloroform, followed by elution with 100% methanol). UV-absorbant (254 nm) fractions were collected, evaporated, and assayed for antibacterial activity by spotting on H-top-agar/LB-agar (Sambrook and Russell, 2001) plates seeded with 10^9 cfu *E. coli* D21f2tolC (Fralick and Burns-Keliher, 1994), incubating 16 h at 37, and assessing growth inhibition. Active fractions eluting at ~5% to ~10% methanol were pooled, further purified by re-chromatography on silica gel (procedures essentially as above), further purified by reversed-phase HPLC [Hitachi 7000 with L7450 detector; Supelco Discovery BIO Wide Pore C18 semi-prep column; 1:1 (v/v) acetonitrile-water isocratic elution; flow rate = 2 ml/min], and evaporated, yielding 80 mg Lpm analog "a3" [MALDI-MS m/z: calculated 1011.41 ($M + Na^+$); found 1011.07] and 8 mg Lpm analog "a2" [MALDI-MS m/z: calculated 1045.59 ($M + Na^+$); found 1044.60, 1046.70]. Material eluting at 100% methanol was further purified by reversed-phase HPLC (procedures essentially as above), and evaporated, yielding 0.2 mg Lpm analog "d1" [MALDI-MS m/z: calculated, 846.98 ($M + Na^+$); found, 847.90].

Lpm analogs: Lpm analog "a1" (4"-O-benzyl-Lpm)

Lpm analog "a1" (4"-O-benzyl-Lpm) was prepared from Lpm by semi-synthesis as follows: To Lpm (Biorbyt: 3 mg; 2.8 µmol) in 50 µl anhydrous dimethylformamide (Sigma-Aldrich), was added anhydrous potassium carbonate (Sigma-Aldrich: 3 mg, 22 µmol), and the reaction mixture was stirred 30 min at 50°C and then allowed to cool to room temperature. An aliquot (10 µl) of 0.28 M benzyl bromide in anhydrous dimethylformamide [2.8 µmol; prepared by dissolving 3.4 µl benzyl bromide (Sigma-Aldrich) in 50 µl anhydrous dimethylformamide immediately before use] was added, and the reaction mixture was stirred 30 min at 50°C. The reaction mixture was evaporated to remove dimethylformamide and then re-suspended in 600 µl 100 mM monobasic sodium phosphate (ThermoFisher). Precipitated solids were collected by centrifugation, rinsed with water, re-dissolved in methanol, and purified by reversed-phase HPLC (Hitachi 2000 with L2455 detector; Phenomenex Luna C18, 100 Å, 25 mm x 4.6 mm column;

phase A = water; phase B = acetonitrile; gradient = 40% B at 0 min, 100% B at 20 min; flow rate = 1 ml/min). Lpm analog "a1" eluted at 20 minutes. Yield: 0.35 mg, 10%. MALDI-MS m/z: calculated, 1171.44 (M + Na+); found 1169.64, 1171.64.

Other RNAP inhibitors

Cor A and Rip A were the kind gift of H. Irschik and R. Jansen (Helmholtz Institut, Braunschweig, Germany), Stl was the kind gift of E. Steinbrecher (Upjohn-Pharmacia, Kalamazoo, MI), and Sal A was the kind gift of W. Fenical (The Scripps Research Institute, La Jolla, CA). Myx B was prepared as in Ebright and Ebright, 2012; GE was prepared as in Ciciliato et al., 2004; and PUM was prepared as in Maffioli et al., 2017. Rif was purchased from Sigma-Aldrich, and CBR was purchased from Maybridge.

***M. tuberculosis* RNAP σ^A holoenzyme**

Mtb RNAP σ^A holoenzyme was prepared as in Lin et al., 2017.

***M. tuberculosis* RNAP core enzyme and σ^A**

For experiments in Figs. S1B, S3D, and S5, *Mtb* RNAP core enzyme and *Mtb* σ^A were prepared as in Lin et al., 2017, but using plasmid pCOLADuet-Mtb-rpoBC [prepared by replacing the NcoI-BamHI segment of plasmid pCOLA-Duet (EMD Millipore) by the NcoI-BamHI segment of a DNA fragment carrying CCATGGTG followed by *Mtb rpoB* codons 3-1174 followed by TAAGGATCC, prepared by PCR using plasmid pJF09 (Rodrigue et al., 2007; gift of S. Rodrigue, Universitė de Sherbrooke, Canada), and then replacing the NdeI-MfeI segment of the resulting plasmid by the NdeI-MfeI segment of a DNA fragment carrying CATATG followed by *Mtb rpoC* codons 2-1316 followed by TAGCAATTG, prepared by PCR using plasmid pJF10 (Rodrigue et al., 2007; gift of S. Rodrigue, Universitė de Sherbrooke, Canada)], or derivatives thereof constructed using site-directed mutagenesis (QuikChange Site-Directed Mutagenesis Kit; Agilent), in place of plasmid pCOLA-rpoB-rpoC (Banerjee et al., 2014).

S. aureus RNAP σ^A holoenzyme

S. aureus RNAP σ^A holoenzyme was prepared as in Maffioli et al., 2017.

E. coli RNAP σ^{70} holoenzyme

For experiments in Figs. S1B and S5, hexahistidine-tagged *E. coli* RNAP σ^{70} holoenzyme was prepared from *E. coli* strain XE54 (Tang et al., 1994) transformed with plasmid pREII-NHα (Tang et al., 1994), using procedures as in Niu et al., 1996.

For experiments in Figs. 4C-F, fluorescent-probe-labelled, hexahistidine-tagged *E. coli* RNAP σ^{70} holoenzyme was prepared using unnatural-amino-acid mutagenesis (Chin et al., 2002) of co-expressed genes encoding RNAP β', β, α, and ω subunits and σ^{70}, yielding an RNAP σ^{70} holoenzyme derivative containing 4-azido-L-phenylalanine (AzF) at position 284 of β' and position 106 of β, followed by azide-specific Staudinger ligation (Saxon and Bertozzi, 2000) to incorporate the fluorescent probes Cy3B and Alexa647 at position 284 of β' and position 106 of β, as follows (Fig. 4A): Single colonies of *E. coli* strain BL21(DE3) (EMD Millipore) co-transformed with plasmid pVS10-rpoB106am;rpoC284am [constructed by use of site-directed mutagenesis (QuikChange Site-Directed Mutagenesis Kit; Agilent) to replace *rpoB* codon 106 and *rpoC* codon 284 by amber codons in plasmid pVS10 (Belogurov et al., 2007)], plasmid pRSFduet-sigma (Hudson et al., 2009), and plasmid pEVOL-pAzF (Chin et al., 2002) were used to inoculate 20 ml LB broth (Sambrook and Russell, 2001) containing 100 μg/ml ampicillin, 50 μg/ml kanamycin, and 35 μg/ml chloramphenicol, and cultures were incubated 16 h at 37°C with shaking. Culture aliquots (2x10 ml) were used to inoculate LB broth (2x1 L; Sambrook and Russell, 2001) containing 2 mM AzF (Chem-Impex International), 100 μg/ml ampicillin, 50 μg/ml kanamycin, and 35 μg/ml chloramphenicol, cultures were incubated with shaking until OD_{600} = 0.6; L-arabinose was added to 0.2% and IPTG was added to 1 mM, and cultures were further incubated 16 h at 16°C with shaking. Cells were harvested by centrifugation (4,000 x g; 20 min at 4˚C), re-suspended in 20 ml buffer A (10

mM Tris-HCl, pH 7.9, 200 mM NaCl, and 5% glycerol), and lysed using an EmulsiFlex-C5 cell disrupter (Avestin). The lysate was cleared by centrifugation (20,000 x g; 30 min at 4°C), precipitated with polymin P (Sigma-Aldrich) as in Niu et al., 1996, and precipitated with ammonium sulfate as in Niu et al., 1996. The sample was dissolved in 30 ml buffer A and loaded onto a 5 ml column of Ni-NTA-agarose (Qiagen) pre-equilibrated in buffer A, and the column was washed with 50 ml buffer A containing 10 mM imidazole and eluted with 25 ml buffer A containing 200 mM imidazole. The sample was further purified by anion-exchange chromatography on Mono Q 10/100 GL (GE Healthcare; 160 ml linear gradient of 300-500 mM NaCl in 10 mM Tris-HCl, pH 7.9, 0.1 mM EDTA, and 5% glycerol; flow rate = 2 ml/min). Fractions containing AzF-derivatized hexahistidine-tagged *E. coli* RNAP σ^{70} holoenzyme were pooled, concentrated to ~1 mg/ml using 30 kDa MWCO Amicon Ultra-15 centrifugal ultrafilters (EMD Millipore), and stored in aliquots at -80°C. A reaction mixture containing 10 μM AzF-derivatized hexahistidine-tagged *E. coli* RNAP σ^{70} holoenzyme, 100 μM Alexa647-pentanoyl-ethylenediaminyl-phosphine (prepared as in Chakraborty et al., 2010, 2015), and 100 μM Cy3B-carboyl-ethylenediaminyl-phosphine (prepared as in Chakraborty et al., 2010, 2015) in 1 ml buffer B (50 mM Tris-HCl, pH 7.9, 100 mM KCl, 5% glycerol, and 2% dimethylformamide) was incubated 1 h at 15°C, incubated 16 h on ice, and subjected to 5 cycles of buffer exchange (dilution with 5 ml buffer B, followed by concentration to 0.5 ml) using 30 kDa MWCO Amicon Ultra-15 centrifugal ultrafilters (EMD Millipore). The sample was further purified by gel-filtration chromatography on HiLoad 16/60 Superdex 200 prep grade (GE Healthcare) pre-equilibrated in buffer C (20 mM Tris-HCl, pH 8.0, 100 mM NaCl, 5 mM MgCl2, 1 mM β-mercaptoethanol, and 5% glycerol) and eluted in buffer C. Fractions containing fluorescent-probe-labelled hexahistidine-tagged *E. coli* RNAP σ^{70} holoenzyme were pooled, concentrated to 1 mg/ml in buffer C using 30 kDa MWCO Amicon Ultra-15 centrifugal ultrafilters (EMD Millipore) and stored in aliquots at -80°C.

For experiments in Fig. 4G, fluorescent-probe-labelled, hexahistidine-tagged, FLAG-tagged *E. coli* RNAP σ^{70} holoenzyme was prepared using unnatural-amino-acid mutagenesis (Chin et al., 2002) of genes

encoding RNAP β' and β subunits to incorporate azidophenylalanine at position 284 of β' and position 106 of β, azide-specific Staudinger ligation (Saxon and Bertozzi, 2000) to incorporate Cy3B at position 284 of the resulting β' derivative and Alexa647 at position 106 of the resulting β derivative, and *in vitro* reconstitution of RNAP (Tang et al., 1995) from the resulting β' and β derivatives, RNAP α and ω subunits, and σ^{70}, as in Chakraborty et al., 2010, 2012, 2015.

Efficiencies of incorporation of fluorescent probes were determined from UV/Vis-absorbance measurements and were calculated as:

$$\text{concentration of product} = [A_{280} - \varepsilon_{Cy3B,280}(A_{Cy3B,559}/\varepsilon_{Cy3B,559}) - \varepsilon_{Alexa,280}(A_{Alexa,652}/\varepsilon_{Alexa647,652})]/\varepsilon_{P,280}$$

$$\text{Cy3B labelling efficiency} = 100\%[(A_{Cy3B,559}/\varepsilon_{Cy3B,559})/(\text{concentration of product})]$$

$$\text{Alexa647 labelling efficiency} = 100\%[(A_{Alexa,652}/\varepsilon_{Alexa,652})/(\text{concentration of product})]$$

where A_{280} is the measured absorbance at 280 nm, $A_{Cy3B,559}$ is the measured absorbance at the long-wavelength absorbance maximum of Cy3B (559 nm), $A_{Alexa,652}$ is the measured absorbance at the long-wavelength absorbance maximum of Alexa647 (652 nm), $\varepsilon_{P,280}$ is the molar extinction coefficient of RNAP σ^{70} holoenzyme at 280 nm (240,000 M^{-1} cm^{-1}), $\varepsilon_{Cy3B,280}$ is the molar extinction coefficient of Cy3B at 280 nm (7,350 M^{-1} cm^{-1}), $\varepsilon_{Alexa,280}$ is the molar extinction coefficient of Alexa647 at 280 nm (10,400 M^{-1} cm^{-1}), and $\varepsilon_{Cy3B,559}$ is the extinction coefficient of Cy3B at its long-wavelength absorbance maximum (130,000 M^{-1} cm^{-1}), and $\varepsilon_{Alexa,652}$ is the extinction coefficient of Alexa647 at its long-wavelength absorbance maximum (245,000 M^{-1} cm^{-1}). Labelling efficiencies were ~90% for Cy3B and ~70% for Alexa647.

Specificities of incorporation of fluorescent probes were determined from the observed labelling efficiencies of (i) the labelling reaction with the AzF-derivatized hexahistidine-tagged *E. coli* RNAP

σ^{70} holoenzyme and (ii) a control labelling reaction with non-AzF-derivatized hexahistidine-tagged *E. coli* RNAP σ^{70} holoenzyme, and were calculated as:

labelling specificity = 100%[1 - [(labelling efficiency with P)/(labelling efficiency with AzF-P)]

where AzF-P is AzF-derivatized hexahistidine-tagged *E. coli* RNAP σ^{70} holoenzyme, and P is non-AzF-derivatized hexahistidine-tagged *E. coli* RNAP σ^{70} holoenzyme. Labelling specificities were >90%.

***T. thermophilus* RNAP core enzyme and RNAP σ^A holoenzyme**

T. thermophilus RNAP core enzyme and RNAP σ^A holoenzyme were prepared as in Zhang et al., 2012.

RNAP-inhibitory activities

Fluorescence-detected RNAP-inhibition assays with the profluorescent substrate γ-[2′-(2-benzothiazoyl)-60-hydroxybenzothiazole]-ATP (BBT-ATP; Jena Bioscience) were perfomed as in Feng et al., 2015, using 75 nM RNAP holoenzyme [*Mtb* RNAP σ^A holoenzyme (prepared by pre-incubating 75 nM *Mtb* RNAP core enzyme or core enzyme derivative and 300 nM *Mtb* σ^A in transcription buffer 10 min at 0°C), *S. aureus* RNAP σ^A holoenzyme, *E. coli* RNAP σ^{70} holoenzyme, or *T. thermophilus* RNAP σ^A holoenzyme] and 20 nM DNA fragment containing bacteriophage T5 N25 promoter (prepared as in Zhang et al., 2014). The transcription buffer for *E. coli* RNAP σ^{70} holoenzyme was 50 mM Tris-HCl (pH 8.0), 100 mM KCl, 10 mM $MgCl_2$, 1 mM DTT, 10 mg/ml bovine serum albumin, and 5.5% glycerol. The transcription buffer for *Mtb* RNAP σ^A holoenzyme, *S. aureus* RNAP σ^A holoenzyme, and *T. thermophilus* RNAP σ^A holoenzyme was 40 mM Tris-HCl (pH 8.0), 75 mM NaCl, 5 mM $MgCl_2$, 2.5 mM DTT, 5% DMSO, and 12.5% glycerol.

Radichemical RNAP-inhibition assays with HeLa nuclear extract (human RNAP I/II/III) were performed as in Degen et al., 2014.

Half-maximal inhibitory concentrations (IC50s) were calculated by non-linear regression in SigmaPlot (Systat Software).

Lpm-resistant mutants

Lpm-resistant mutants were isolated using procedures analogous to those used for isolation of Myx-resistant mutants in Mukhopadhyay et al., 2008. Mutagenesis reactions were performed using the QuikChange Site-Directed Mutagenesis Kit (Agilent) with *E. coli rpoC* plasmid pRL663 (Wang et al., 1995) and oligodeoxyribonucleotide forward and reverse primers corresponding to *rpoC* codons 1-20, 67-68, 77-81, 93-100, 245-256, 259-265, 325-355, 378-382, 393-403, 425-433, 466-481, 1319-1327, and 1347-1360, or with *E. coli rpoB* plasmid pRL706 (Severinov et al., 1997) and oligodeoxyribonucleotide forward and reverse primers corresponding to *rpoB* codons 854-857, 890-899, 914-922, and 1246-1342 (primers at 75 nM; all other components at concentrations as specified by the manufacturer). Mutagenized plasmid DNA was introduced by transformation into *E. coli* XL1-Blue (Agilent). Transformants (~10^4 cells) were applied to LB-agar (Sambrook and Russell, 2001) plates containing 200 μg/ml ampicillin, plates were incubated 16 h at 37°C, and plasmid DNA was prepared from the pooled resulting colonies. The resulting pooled mutagenized plasmid DNA was introduced by transformation into uptake-proficient, efflux-deficient *E. coli* strain D21f2tolC (Fralick and Burns-Keliher, 1994). Transformants (~10^3 cells) were applied to LB-agar plates containing 5 μg/ml Lpm (the minimal concentration that prevents colony formation by wild-type transformants), 200 μg/ml ampicillin, and 1 mM IPTG, and plates were incubated 24-48 h at 37°C. Lpm-resistant mutants were identified by the ability to form colonies on this medium, were confirmed by re-streaking on the same medium, and were demonstrated to contain plasmid-linked Lpm-resistant mutations by preparing plasmid DNA,

transforming *E. coli* D21f2tolC with plasmid DNA, and plating transformants on the same medium. Nucleotide sequences of *rpoB* and *rpoC* were determined by Sanger sequencing (eight primers per gene).

Resistance and cross-resistance levels

Experiments in Fig. 2C and S6B-C assessing resistance and cross-resistance levels of Lpm-resistant *E. coli* D21f2tolC pRL706 and *E. coli* D21f2tolC pRL663 derivatives (preceding section) and Myx/Cor/Rip-resistant *E. coli* D21f2tolC pRL706 and *E. coli* D21f2tolC pRL663 derivatives (Mukhopadhyay et al., 2008) were performed using spiral gradient endpoint assays (Wallace and Corkill, 1989; Paton et al., 1990; Schalkowsky, 1994) on 150 mm x 4 mm exponential-gradient plates containing LB agar (Sambrook and Russell, 2001), 0.05-50 μg/ml test compound (Lpm, Rif, Myx, Cor, or Rip), 200 mg/ml ampicillin, and 1 mM IPTG. Test compounds were applied to plates using an Autoplate 4000 spiral plater (Spiral Biotech). Single colonies of transformants of *E. coli* D21f2tolC (Fralick and Burns-Keliher, 1994) were inoculated into 5 ml LB broth (Sambrook and Russell, 2001) containing 200 μg/ml ampicillin and incubated at 37°C with shaking until OD_{600} = 0.4-0.6, IPTG was added to 1 mM, and cultures were incubated 1 h at 37°C with shaking. Diluted aliquots (~$1x10^9$ cfu/ml for Fig. 2C and ~$1x10^8$ cfu/ml for Fig. S6B) were swabbed radially onto plates, and plates were incubated 16 h at 37°C. For each culture, the streak length was measured using a clear plastic template (Spiral Biotech), the test-compound concentration at the streak endpoint was calculated using the program SGE: Spiral Gradient Endpoint (v1.3; Spiral Biotech), and the minimum inhibitory concentration (MIC) was defined as the test-compound concentration at the streak endpoint.

Experiments in Fig. 2D assessing resistance and cross-resistance levels of chromosomal Lpm-resistant mutants [mutations transferred from pRL706 or pRL663 derivatives of preceding section to chromosome of *E. coli* D21f2tolC (Fralick and Burns-Keliher, 1994) by λ-Red-mediated recombineering (procedures essentially as in Datsenko and Wanner, 2000, but using transformation rather than electroporation)] were performed using broth microdilution assays (Clinical and Laboratory Standards Institute, 2009). Single

colonies were inoculated into 5 ml LB broth (Sambrook and Russell, 2001) and incubated at 37°C with shaking until OD_{600} = 0.4-0.8. Diluted aliquots (~$5x10^4$ cells) in 97 µl LB broth were dispensed into wells of a 96-well plate, and were supplemented with 3 µl methanol or 3 µl of a 2-fold dilution series of Lpm ($MIC_{wild\text{-}type}$ = 1.56 µg/ml), Rif ($MIC_{wild\text{-}type}$ = 0.20 µg/ml), CBR ($MIC_{wild\text{-}type}$ = 6.25 µg/ml), Sal ($MIC_{wild\text{-}type}$ = 0.049 µg/ml), Stl ($MIC_{wild\text{-}type}$ = 3.13 µg/ml), or Myx ($MIC_{wild\text{-}type}$ = 0.20 µg/ml), in methanol (final concentrations = 0 and 0.006-50 µg/ml), or diluted aliquots (~$1x10^5$ cells) in 50 µl LB broth were supplemented with 50 µl LB broth or 50 µl of a 2-fold dilution series of GE ($MIC_{wild\text{-}type}$ = 500 µg/ml) or PUM ($MIC_{wild\text{-}type}$ = 400 µg/ml) in LB broth (final concentrations = 0 and 25-2000 µg/ml). Plates were incubated 16 h at 37°C. The MIC was defined as the lowest tested concentration that inhibited bacterial growth by ≥90%.

Experiments in Fig. 2E assessing Lpm-cross-resistance levels of Rif-, GE/PUM-, and Sal-resistant mutants were performed as described for experiments in Fig. 2D, but analyzing a panel of *E. coli* D21f2tolC derivatives (Degen et al., 2014; Zhang et al., 2014; Maffioli et al., 2017) comprising 4 chromosomal Rif-resistant mutants, 3 chromosomal GE/PUM-resistant mutants, and 5 chromosomal Sal-resistant mutants.

Experiments in Fig. 2E assessing Lpm-cross-resistance levels of CBR- and Stl-resistant mutants were performed essentially as described for experiments in Fig. 2D, but analyzing a panel of *E. coli* D21f2tolC pRL706 and *E. coli* D21f2tolC pRL663 derivatives (Tuske et al., 2005; Feng et al., 2015) comprising 5 CBR-resistant mutants and 5 Stl-resistant mutants. Single colonies were inoculated into 5 ml LB broth (Sambrook and Russell, 2001) containing 200 µg/ml ampicillin and incubated at 37°C with shaking until OD_{600} = 0.4-0.6, IPTG was added to 1 mM, and cultures were incubated 1 h at 37°C with shaking. Diluted aliquots (~$5x10^4$ cells) in 97 µl LB broth containing 200 µg/ml ampicillin and 1 mM IPTG were dispensed into wells of a 96-well plate, and were supplemented with 3 µl methanol or 3 µl of a 2-fold dilution series of CBR or Stl in methanol and further processed as described for experiments in Fig. 2D.

Checkerboard interaction assays

Antibacterial activities of combinations of Lpm and Rif were assessed in checkerboard interaction assays (White et al., 1996; Meletiadis et al., 2010). Broth-microdilution assays (procedures as described in the preceding section for determination of resistance levels of chromosomal Lpm-resistant mutants) were performed in checkerboard format, using *E. coli* D21f2tolC (Fralick and Burns-Keliher, 1994) and using LB broth (Sambrook and Russell, 2001) containing all pairwise combinations of: (i) Lpm at 2.0x, 1.75x, 1.5x, 1.3125x, 1.25x, 1.125x, 0.9375x, 0.75x, 0.5625x, 0.5x, 0.375x, 0.25x, and 0.1875x MIC_{Lpm} and (ii) Rif at 2.0x, 1.75x, 1.5x, 1.3125x, 1.25x, 1.125x, 0.9375x, 0.75x, 0.5625x, 0.5x, 0.375x, 0.25x, and 0.1875x MIC_{Rif}. Fractional inhibitory concentrations (FICs), FIC indices (FICIs), and minimum and maximum FICIs ($FICI_{min}$ and $FICI_{max}$) were calculated as in Meletiadis et al., 2010. $FICI_{min} \leq 0.5$ was deemed indicative of super-additivity (synergism), $FICI_{min} > 0.5$ and $FICI_{max} \leq 4.0$ was deemed indicative of additivity, and $FICI_{max} > 4.0$ was deemed indicative of sub-additivity (antagonism) (White et al., 1996; Meletiadis et al., 2010).

Cryo-EM structure determination (*M. tuberculosis* RNAP-Lpm): sample preparation

Lacey carbon grids (LC300-CU-100; Electron Microscopy Sciences) were glow-discharged for 30 s using a glow-discharge cleaning system (PELCO easiGlow; Ted Pella) and mounted in the sample chamber of an EM GP grid plunger (Leica) at 18ºC and relative humidity = 95%. Grids were spotted with 3.5 µl 1 µM *Mtb* RNAP-Lpm and 50 µM Lpm in 20 mM Tris-HCl, pH 8.0, 75 mM NaCl, 5 mM $MgCl_2$, 5 mM dithiothreitol, and 0.1% n-octyl-β-D-glucopyranoside [prepared by pre-equilibrating 150 µl samples containing components other than n-octyl-β-D-glucopyranoside (Biosynth) 30 min at 25°C, and adding n-octyl-β-D-glucopyranoside immediately before spotting], incubated 10 s, blotted with filter paper (Whatman Grade 541; Sigma-Aldrich) for 2.3 s, flash-frozen by plunging in liquid ethane cooled with liquid nitrogen, and stored in liquid nitrogen.

Cryo-EM structure determination (*M. tuberculosis* RNAP-Lpm): data collection and data reduction

Data were collected at the National Resource for Automated Molecular Microscopy of the Simons Electron Microscopy Center using a 300 keV Titan Krios (FEI/ThermoFisher) electron microscope equipped with a K2 Summit direct electron detector (Gatan) operating in counting mode and a GIF Quantum imaging filter (Gatan) with slit width of 20 eV. Data were collected semi-automatically using the software package Leginon (Suloway et al., 2005), a nominal magnification of 130,000x, a calibrated pixel size of 1.061 Å, and a dose rate of 8 electrons/pixel/s. Movies were recorded at 200 ms/frame for 10 s (50 frames total), resulting in a total radiation dose of 72.05 electrons/Å^2 per movie Defocus range was varied between 1.0 μm and 2.0 μm. A total of 2,458 micrographs were recorded from two grids over 2 days.

Data were processed as summarized in Fig. S1C-E. Data processing was performed on an Ubuntu 16.04 Linux GPU workstation (Titan Computers) containing four GeForce GTX 1080 Ti graphic cards (Nvidia; Kimanius et al., 2016). Frames in individual movies were aligned using MotionCor2 (Zheng et al., 2017), and the first 35 frames per movie were merged to calculate individual micrographs.

Contrast-transfer-function estimations were performed using Gctf (Zhang, 2016), yielding defocus-range estimates ranging from 0.4 μm to 4.0 μm for individual micrographs. Initial particle picking was performed on 25 selected micrographs from the first grid (8,609 particles) using the Xmipp routine of the software package Scipion v1.1 (de la Rosa-Trevín et al., 2016), and particles were used for two-dimensional class averaging in Relion v2.0.5 (Fernandez-Leiro and Scheres, 2017). Eight distinct two-dimensional classes were selected as templates for picking 452,912 particles from 1,236 selected micrographs from the first grid and 366,594 particles from 1,025 selected micrographs from the second grid, using the Autopick routine of Relion. Two- and three-dimensional classifications were performed on the 452,912 particles from the first grid and 366,594 particles from the second grid, using Relion and using a 60 Å low-pass-filtered map calculated from the crystal structure of *Mtb* RPo (PDB: 5UH5; Lin et al., 2017; protein residues only) as the starting reference model for three-dimensional classification. Following identification and removal of heterogeneous particles in the two- and three-dimensional

classifications, independent but similar density maps were obtained from 126,977 particles from the first grid and 97,412 particles from the second grid. Following merging of the 224,389 particles from the first and second grids, three-dimensional auto-refinement using Relion, and local angular sampling using Relion, a final density map was obtained from a subset of 68,895 particles. Gold-standard Fourier-shell-correlation analysis (FSC; Henderson et al., 2012) indicated a mean map resolution of 3.52 Å, and ResMap (Kucukelbir et al., 2014) indicated a median map resolution of 3.5 Å (Fig. S1F-G; Table 1). The initial atomic model for protein residues of *Mtb* RNAP-Lpm was built by manual rigid-body fitting of RNAP β', RNAP β, RNAP α^{I}, RNAP α^{II}, RNAP ω , and σ segments from the crystal structure of *Mtb* RPo (PDB: 5UH5; Lin et al., 2017; protein residues only) into the cryo-EM density map in Coot (Emsley et al., 2010), followed by adjustment of backbone and sidechain conformations in Coot. For σR4 (residues 464-528), density was weak, suggesting high segmental flexibility; σR4 was fitted as a rigid-body segment and was not further adjusted. For the RNAP β' N and C-termini (residues 1-2 and 1282-1316), the central part of the RNAP β' trigger loop (residues 1014-1022), the RNAP β N and C-termini (residues 1-27 and 1145-1172), the RNAP α^{I} N-terminus and C-terminal domain (residues 1-2 and 227-347), the RNAP α^{II} N-terminus and C-terminal domain (residues 1-2 and 233-347), the RNAP ω N-terminus (residues 1-27), σR1.1 (residues 1-224), and a loop and short extended segment of the σR3-σR4 linker (residues 426-433 and 443-445), density was absent, suggesting very high segmental flexibility; these segments were not fitted. The initial atomic model for Lpm atoms of *Mtb* RNAP-Lpm was built by manual rigid-body fitting of a crystal structure of Lpm (CCDC 114782; Ihle et al., 2000) into the cryo-EM density map using Coot, followed by torsion-angle adjustments using Coot. Iterative cycles were performed of real-space model building in Coot followed by reciprocal-space fitting to structure-factor amplitudes and phases calculated from the cryo-EM density map in Phenix (Adams et al., 2010). The final atomic model, with map-to-model correlation of 0.83, was deposited in the Electron Microscopy Data Bank (EMDB) and Protein Data Bank (PDB) with accession codes EMDB: 4230 and PDB: 6FBV (Table 1).

Crystal structure determination (*T. thermophilus* RNAP core enzyme): sample preparation

Robotic crystallization trials were performed for *T. thermophilus* RNAP core enzyme using a Gryphon liquid handling system (Art Robbins Instruments), commercial screening solutions (Emerald Biosystems, Hampton Research, and Qiagen), and the sitting-drop vapor-diffusion technique (drop: 0.2 µl RNAP plus 0.2 µl screening solution; reservoir: 60 µl screening solution; 22°C). 900 conditions were screened. Rod-like crystals appeared under the identified crystallization conditions [0.1 M Hepes-NaOH, pH 7.5, 20 mM $MgCl_2$, and 22% poly(acrylic acid sodium salt), 5,100 Da (Hampton Research); 22°C] within two weeks. Crystals were transferred from the sitting drop to a reservoir solution containing 20% (v/v) ethylene glycol (Sigma-Aldrich) and flash-cooled by immersing in liquid nitrogen.

Crystal structure determination (*T. thermophilus* core enzyme): data collection and data reduction

Diffraction data and selenium single-wavelength anomalous dispersion data were collected from cryo-cooled crystals at Argonne Photon Source beamline 19ID-D. Data were processed using HKL2000 (Otwinowski and Minor, 1997). The resolution cut-off criteria were $I/\sigma > 1.1$ and $R_{merge} < 1$.

The structure of T. *thermophilus* RNAP core was solved by molecular replacement with Molrep (Vagin and Teplyakov, 1997) using PDB: 4GZY (Weixlbaumer et al., 2013) as the search model. One RNAP molecule was present in the asymmetric unit. Early-stage refinement included rigid-body refinement of RNAP, followed by rigid-body refinement of RNAP subunits, followed by rigid-body refinement of 44 RNAP domains (methods as in Zhang et al., 2012). Cycles of iterative model building with Coot (Emsley et al., 2010) and refinement with Phenix (Adams et al., 2010) were performed. Improvement of the coordinate model resulted from improvement of phasing. The final model was generated by XYZ-coordinate refinement with secondary-structure restraints in Phenix, followed by group B-factor and individual B-factor refinement in Phenix. The final model, refined to R_{work} and R_{free} of 0.22 and 0.27, respectively, was deposited in the PDB with accession code PDB: 6ASG (Table 2).

Single-molecule FRET: sample preparation

Observation wells were prepared essentially as described (Duchi et al., 2016, 2017; Fig. 4B): Borosilicate glass coverslips (#1.5; Menzel/ThermoFisher) were incubated in 40 ml acetone 5 min at 22°C, incubated in 40 ml 2% (v/v) Vectabond aminosilane reagent (Vector Labs) in acetone 5 min at 22°C, washed with 100 ml water at 22°C, dried under nitrogen, and bonded to CultureWell 6 mm silicone gaskets (GBL103280; Grace Bio-Labs), yielding 30 μl wells containing aminosilane-functionalized glass floors. Aliquots (20 μl) of 30 mM methoxy-PEG succinimidyl valerate (mPEG-SVA, MW 5,000; Laysan Bio) and 0.75 mM biotinyl-PEG succinimidyl valerate (Biotin-PEG-SVA, MW 5,000; Laysan Bio) in 50 mM MOPS-NaOH, pH 7.5, were added to wells and incubated 90 min at 22°C, supernatants were removed, and wells were washed with 5x200 μl PBS (0.01 M sodium phosphate, pH. 7.4, 137 mM NaCl, and 2.7 mM KCl), yielding wells with biotin-PEG/mPEG-functionalized borosilicate glass floors. Aliquots (30 μl) of 10 μM NeutrAvidin (ThermoFisher) in 0.5xPBS then were added to wells and incubated 10 min at 22°C, supernatants were removed, and wells were washed with 3x100 μl PBS, yielding wells with NeutrAvidin-biotin-PEG/PEG-functionalized glass floors. Aliquots (30 μl) of 40 nM biotinylated anti-hexahistidine monoclonal antibody (Penta-His Biotin Conjugate; Qiagen) in buffer KG7 (40 mM Hepes-NaOH, pH 7.0, 100 mM potassium glutamate, 10 mM $MgCl_2$, 1 mM dithiothreitol, 100 μg/ml bovine serum albumin, and 5% glycerol) then were added to wells and incubated 10 min at 22°C, supernatants were removed, and wells were washed with 3x100 μl KG7, yielding wells with (biotinylated anti-hexahistidine monoclonal antibody)-NeutrAvidin-biotin-PEG/mPEG-functionalized glass floors.

For experiments in Fig. 4C-F, fluorescent-probe-labelled, hexahistidine-tagged *E. coli* RNAP σ^{70} holoenzyme was immobilized in observation wells containing (biotinylated anti-hexahistidine monoclonal antibody)-Neutravidin-biotin-PEG/mPEG-functionalized glass floors (Fig. 4B) as follows: Aliquots (30 μl) of 0.1 nM fluorescent-probe-labelled. hexahistidine-tagged *E. coli* RNAP σ^{70} holoenzyme and 0 or 20 μM (2.5xIC50) Lpm in KG7 (prepared by pre-equilibrating 50 nM fluorescent-probe-labelled.

hexahistidine-tagged *E. coli* RNAP σ^{70} holoenzyme and 0 or 20 μM Lpm in KG7 10 min at 37°C, and then diluting 1:500 with 0 or 20 uM Lpm in KG7 at 37°C) were added and incubated 2-4 min at 22°C, supernatants were removed, wells were washed with 2x30 μl KG7, and 30 μl KG7 containing 2 mM Trolox (Sigma-Aldrich) and an oxygen scavenging system [12.5 μM glucose oxidase (Sigma-Aldrich), 16 nM catalase (C30; Sigma-Aldrich), and 8 mM D-glucose] at 22°C was added. Immobilization densities typically were ~30 molecules per 10 μm x 12 μm field of view. Immobilization specificities typically were >98% (assessed in control experiments omitting biotinylated anti-hexahistidine monoclonal antibody).

For experiments in Fig. 4G, fluorescent-probe-labelled, hexahistidine-tagged *E. coli* RNAP σ^{70} holoenzyme was immobilized in observation wells containing (biotinylated anti-hexahistidine monoclonal antibody)-Neutravidin-biotin-PEG/mPEG-functionalized glass floors in the absence of Lpm as described above, and 3 μl 200 μM Lpm in the same buffer was added during data acquisition [Lpm final concentration = 20 μM (2.5xIC50)].

Single-molecule FRET: data collection and data analysis

FRET experiments were performed on an objective-type total-internal-reflection (TIRF) microscope (Holden et al., 2010; Duchi et al., 2016, 2017). Light from a green laser (532 nm; Samba; Cobolt) and a red laser (635 nm; CUBE 635-30E; Coherent) was combined using a dichroic mirror, coupled into a fiber-optic cable, focused onto the rear focal plane of a 100x oil-immersion objective (numerical aperture 1.4; Olympus), and displaced off the optical axis such that the incident angle at the oil-glass interface of a stage-mounted observation chamber was greater than the critical angle, thereby creating an exponentially decaying evanescent wave. Alternating-laser excitation (ALEX; Kapanidis et al., 2004) was implemented by directly modulating the two lasers using an acousto-optical modulator (1205C; Isomet). Fluorescence emission was collected from the objective, separated from excitation light by a dichroic mirror (545 nm/650 nm; Semrock) and emission filters (545 nm LP, Chroma; and 633/25 nm notch filter, Semrock),

focussed on a slit to crop the image, and then spectrally separated using a dichroic mirror (630 nm DRLP; Omega) into donor and emission channels focused side-by-side onto an electron-multiplying charge-coupled device camera (EMCCD; iXon 897; Andor Technology). A motorized x/y-scanning stage with continuous reflective-interface feedback focus (MS-2000; ASI) was used to control the sample position relative to the objective.

For experiments in Fig. 4C-F, laser powers were 3.5 mW (532 nm laser) and 0.7 mW (635 nm laser), and data were collected for 20 s using a frame rate of 1 frame per 20 ms. For experiments in Fig. 4G, laser powers were 0.5 mW (532 nm laser) and 0.15 mW (635 nm laser), and data were collected for 50 s using a frame rate of 200 ms.

Fluorescence emission intensities in donor (green) and acceptor (red) emission channels were detected using the peak-finding algorithm of the MATLAB (MathWorks) software package TwoTone-ALEX (Holden et al., 2010), as in Holden et al., 2010. Peaks detected in both emission channels (i.e., peaks for molecules containing both donor and acceptor probes) and meeting ellipticity and distance-to-nearest-neighbor thresholds (i.e., ellipticity ≤ 0.6 and distance-to-nearest-neighbor ≥ 6 pixels) were fitted with two-dimensional Gaussian functions to extract background-corrected intensity-vs.-time trajectories for donor emission intensity upon donor excitation (I_{DD}), acceptor emission intensity upon donor excitation (I_{DA}), and acceptor emission intensity upon acceptor excitation (I_{AA}) (Fig. 4C, top), as described (Holden et al., 2010). Intensity-vs.-time trajectories were curated to exclude trajectories exhibiting I_{DD} <300 or >2,000 counts or I_{AA} <200 or >2,000 counts, trajectories exhibiting multiple-step donor or acceptor photobleaching, trajectories exhibiting donor or acceptor photobleaching in frames 1-50, and trajectories exhibiting donor or acceptor photoblinking, and to exclude portions of traces following donor or acceptor photobleaching.

Intensity-vs.-time trajectories were used to calculate trajectories of apparent donor-acceptor FRET efficiency (E*) and donor-acceptor stoichiometry (S) (Fig. 4C, bottom), as described (Kapanidis et al., 2004 and Lee et al., 2005):

$E^* = I_{DA}/(I_{DD} + I_{DA})$

$S = (I_{DA} + I_{DD})/(I_{DD} + I_{DA} + I_{AA})$

E*-vs.-S plots were prepared, S values were used to distinguish species containing only donor, only acceptor, and both donor and acceptor, and E* histograms were prepared for species containing both donor and acceptor, as described (Kapanidis et al., 2004; Lee et al., 2005).

E*-vs. time trajectories that on visual inspection exhibited transitions between distinct E* states (dynamic E*-vs.-time trajectories; ~34%; N = 207) were analyzed globally to identify E* states by use of Hidden Markov Modelling (HMM) with an empirical Bayesian as implemented in the MATLAB (MathWorks) software package ebFRET (van de Meent et al., 2014), essentially as described (van de Meent et al., 2014; Duchi et al., 2016, 2017). E*-vs.-time trajectories were fitted to HMM models with two, three, four, five, or six distinct E* states; the mean scoring parameter L (lower bound per trajectory) was extracted for each model. and the model with three distinct E* states was found to best describe the data (Fig. 4D, right; L = 536, 538, 537, 537 and 537 for models with two, three, four, five, and six states). E* values from the three-state HMM model were extracted, plotted using Origin (OriginLab), and fitted to Gaussian distributions using Origin (Fig 4D, left, colored curves). The resulting histograms provide equilibrium population distributions of E* states and, for each E* state, define mean E* (Fig 4D, left, colored curves and inset).

Dwell times for E* states were extracted from E*-vs.-time trajectories exhibiting >3 transitions between E* states and were plotted as histograms in Origin. The resulting dwell-time histograms were fit with single-exponential functions, and mean dwell times were extracted (Fig. 4F).

E* values were corrected, and accurate donor-acceptor efficiencies (E) and donor-acceptor distances (R) were calculated, as follows (Lee et al., 2005).

$C_1 = E^*_{DO}/ (1- E^*_{DO})$

$C_2 = S_{AO}/ (1- S_{AO})$

$E = [1 - C_2\{(1-S)/S\} - C_1(1-E^*)/E^*\}]/ [\{(1-E^*)/E^*\} + 1 - C_2\{(1-S)/S\}] /$

$[\gamma - (\gamma - 1)[1 - C_2\{(1-S)/S\} - C_1\{(1-E^*)/E^*\}]/ [\{(1-E^*)/E^*\} + 1 - C_2\{(1-S)/S\}]$

$R = R_0 [(1/E)-1]^{1/6}$

where, C_1 is "cross-talk" from leakage of donor emission into the acceptor-emission channel, C_2 is "cross-talk" from direct excitation of the acceptor by the green laser, γ is the detection factor [1 in this work; determined as $\gamma = \Delta I_{AA}/\Delta I_{DD}$, where ΔI_{AA} and ΔI_{DD} are changes in I_{AA} and I_{DD} upon acceptor photobleaching (Ha et al., 1999)], E^*_{DO} is E* of the donor-only subpopulation, S_{AO} is S of the acceptor-only subpopulation, and R_0 is the Főrster parameter [60.1 Å in this work; calculated as: $R_0 = 9780(n^{-4}\kappa^2 Q_D J)^{1/6}$ Å, where n is the refractive index of the medium, κ^2 is the orientation factor relating donor emission dipole and acceptor excitation dipole (approximated as 2/3, noting that all mean E values are <0.5; Wu and Brand, 1992), Q_D is the quantum yield of the donor in the absence of acceptor, and J is the overlap integral of donor emission spectrum and acceptor excitation spectrum].

RNAP clamp angles were determined from E values using the plot of RNAP clamp angle vs. E in Fig. 1 of Chakraborty et al., 2012.

QUANTITATION AND STATISTICAL ANALYSIS

Data for RNAP-inhibitory activities, resistance, and cross-resistance are means of at least two technical replicates

DATA AVAILABILITY

The cryo-EM map and atomic coordinates for the cryo-EM structure of *Mtb* RNAP-Lpm have been deposited in the EMDB and PDB with accession codes EMDB: 4230 and PDB: 6FBV. Atomic coordinates and structure factors for the crystal structure of *T. thermophilus* RNAP core enzyme have been deposited in the PDB with accession code PDB: 6ASG.

SUPPLEMENTARY FIGURES

Figure S1 (related to Fig. 1). Structure of *Mtb* RNAP-Lpm: structure determination

A, Structure of lipiarmycin A3 (Lpm; Arnone et al., 1987). Atom numbering as in Arnone et al., 1987. **B**, RNAP inhibition by Lpm. **C**, Summary of structure-determination procedures. **D**, Representative electron micrograph. **E**, Representative two-dimensional classes. **F**, Fourier-shell-correlation (FSC) analysis. **G**, Resolution distribution.

Figure S2 (related to Fig. 1). Structure of *Mtb* RNAP-Lpm: structure quality

A, Slice through density map of *Mtb* RNAP-Lpm at level of Lpm (left) and portion of slice comprising Lpm (right), colored by local resolution. View orientation as in Fig. 1. **B**, Structure of *Mtb* RNAP-Lpm colored by B-factor. View orientation as in **A**. **C**, Density maps for structural elements of central portion of *Mtb* RNAP-Lpm [two structural elements from RNAP active-center region (first and second panels) and two structural elements from RNAP clamp and RNAP switch region (third and fourth panels)]. Gray mesh, density map; gray, red, and green sticks, carbon, oxygen and nitrogen atoms; violet sphere, RNAP active-center catalytic Mg^{2+}. **D**, Density map for Lpm binding site (stereodiagram). Cyan and green sticks, Lpm carbon and chloride atoms; black dashed lines, H-bonds. Other colors as in **C**.

Figure S3 (related to Fig. 1). Structure of Mtb RNAP-Lpm: RNAP-Lpm interactions

A, Stereoview of density and atomic model for Lpm in *Mtb* RNAP-Lpm (green mesh and cyan sticks), superimposed on atomic models for Lpm from crystal structures of Lpm alone (yellow and green sticks; CCDC 114782 and CCDC 1481503). **B**, Stereoview of inferred RNAP-Lpm interactions. Image extends information in Fig. 1D by including density and fit for interfacial water molecules (blue mesh and pink spheres) and annotations for RNAP structural elements (SW2, SW3, SW4, βa16α1, β'a4α1, and β'a8). **C**, Summary of inferred RNAP-Lpm interactions. Image extends information in Fig. 1E by including interfacial water molecules ("W") and indicating solvent exposure of the Lpm C4" hydroxyl and C5"

chlorine. **D**, Effects of alanine substitution of RNAP residues inferred to make H-bonds with Lpm. $IC50_{WT}$ = 0.3 μM. Residues in **B-D** are numbered as in *Mtb* RNAP and, in parentheses, as in *E. coli* RNAP.

Figure S4 (related to Fig. 1). Sequence alignments and species selectivity of inhibition

A-B, Locations of residues that contact Lpm in sequences of RNAP β subunit (**A**) and RNAP β' subunit (**B**). Sequence alignments for the β and β' subunits of bacterial RNAP (top 20 sequences in each panel) and corresponding subunits of human RNAP I, RNAP II, and RNAP III (bottom three sequences in each panel), showing locations of RNAP residues that contact Lpm (black rectangles; identities from Figs. 1D-E and S3B-C), RNAP switch-region SW2-SW4 (first row of black bars; boundaries as in Cramer et al., 2001), and RNAP conserved regions and conserved structural elements (second and third rows of black bars; boundaries as in Sweetser et al., 1987, Jokerst et al., 1989, and Lane and Darst, 2010). Species are as follows: *Mycobacterium tuberculosis* (MYCTU), *Clostridium difficile* (CDIFF), *Staphylococcus aureus* (STAAU), *Staphylococcus epidermidis* (STAEQ), *Enterococcus faecalis* (ENTFA), *Streptococcus pyogenes* (STRP1), *Streptococcus pneumoniae* (STRP2), *Escherichia coli* (ECOLI), *Salmonella typhimurium* (SALTY), *Klebsiella pneumoniae* (KLEP7), *Enterococcus cloacae* (ENTCC), *Vibrio cholerae* (VIBCH), *Haemophilus influenzae* (HAEIN), *Neisseria gonorrhoeae* (NEIG1), *Stenotrophomonas maltophilia* (STPMP), *Moraxella catarrhalis* (MORCA), *Acinetobacter baumannii* (ACIBC), *Pseudomonas aeruginosa* (PSEAE), *Thermus thermophilus* (THETH), *Thermus aquaticus* (THEAQ), *Deinococcus radiodurans* (DEIRA), and *Homo sapiens* (HUMAN). **c**, Absence of inhibition of human RNAP I, RNAP II, and RNAP III by Lpm.

Figure S5 (related to Fig. 1). Structure-activity relationships for Lpm analogs

A, Structures of Lpm analogs. Compound "a"1 is Lpm (Arnone et al., 1987). Compounds "a3"-"c1" and "e1" are previously known Lpm analogs (Babakhani et al., 2011; Hochlowski et al., 1997; Xiao et al.,

2011; Niu et al., 2011). Compounds "a1"-"a2" and ""d1" are Lpm analogs of this report (see Methods). **B**, RNAP-inhibitory activities of Lpm analogs. $IC50_{LPM}$ is 0.3 μM for *Mtb* RNAP σ^A holoenzyme, 0.9 μM for *Staphylococcus aureus* RNAP σ^A holoenzyme, and 8 μM for *Escherichia coli* RNAP σ^{70} holoenzyme.

Figure S6 (related to Fig. 2). Lpm-resistance and cross-resistance

A, Stereodiagram of RNAP-Lpm interactions, showing RNAP structural elements SW2, SW3, SW4, βa16α1, and β'a4α1, and showing amino acids at which substitutions conferring high-level (≥4-fold) Lpm-resistance are obtained (sequences from Fig. 2C). Gray ribbons, RNAP; cyan, Lpm; red, resistance sites. **B**, Comprehensive analysis of cross-resistance of Lpm-resistant mutants (sequences from Fig. 2C) to Rif, Myx, Cor, and Rip. **C**, Comprehensive analysis of cross-resistance of Myx-, Cor-, and Rip-resistant mutants to Lpm. [Substitution of RNAP β1123 (1325) to Leu previously was reported to confer resistance to Myx, Cor, and Rip, but re-analysis indicates no resistance to Myx, Cor, and Rip.] Residues in **B-C** are numbered as in *Mtb* RNAP and, in parentheses, as in *E. coli* RNAP.

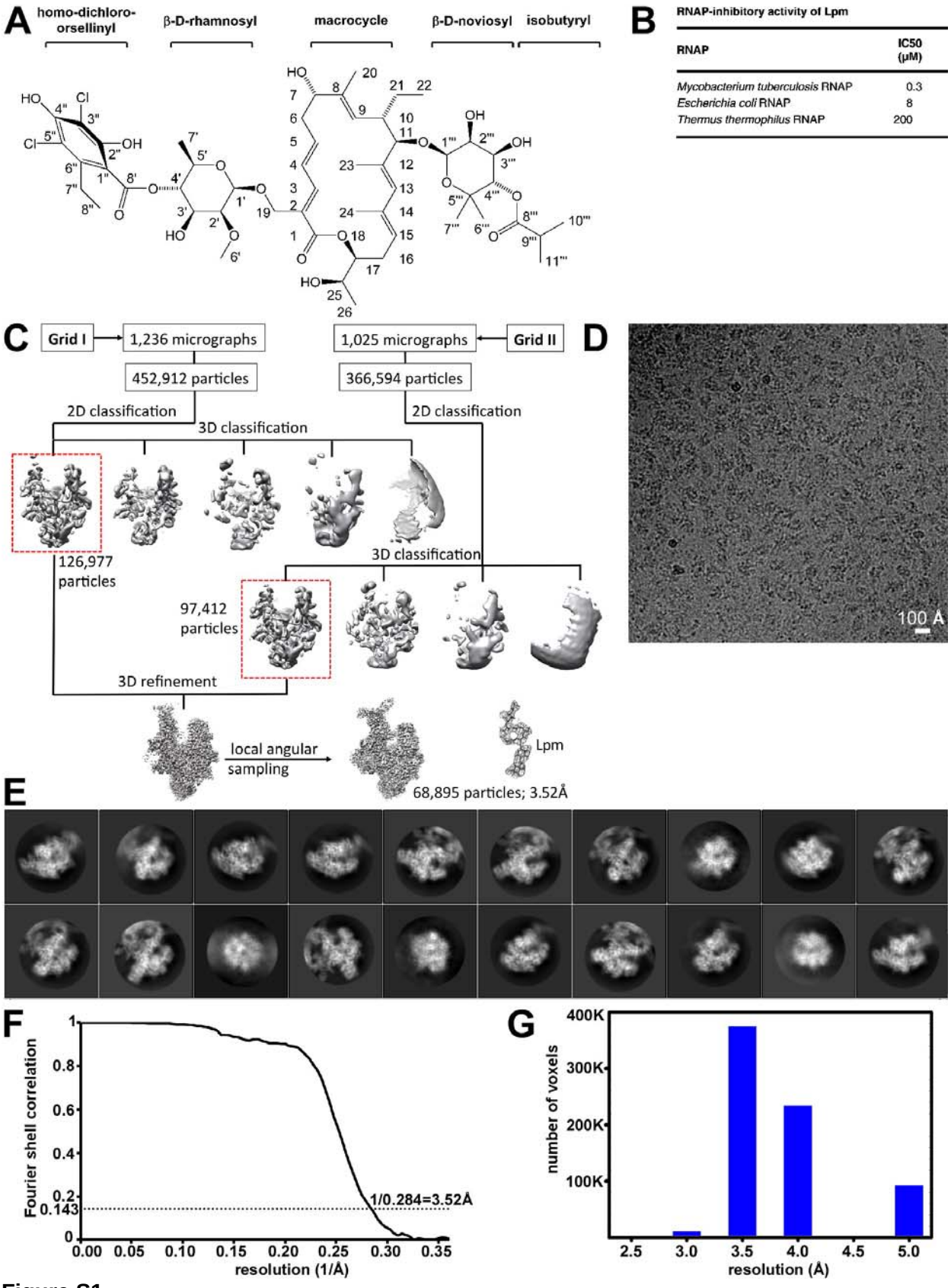
A
homo-dichloro-orsellinyl
β-D-rhamnosyl
macrocycle
β-D-noviosyl
isobutyryl
B
RNAP-inhibitory activity of Lpm
RNAP
IC50 (μM)
Mycobacterium tuberculosis RNAP 0.3
Escherichia coli RNAP 8
Thermus thermophilus RNAP 200
C
Grid I
1,236 micrographs
452,912 particles
2D classification
3D classification
126,977 particles
3D refinement
Grid II
1,025 micrographs
366,594 particles
2D classification
3D classification
97,412 particles
local angular sampling
Lpm
68,895 particles; 3.52Å
D
100 Å
E
F
Fourier shell correlation
1/0.284=3.52Å
0.143
resolution (1/Å)
G
number of voxels
400K
300K
200K
100K
resolution (Å)

Figure S1

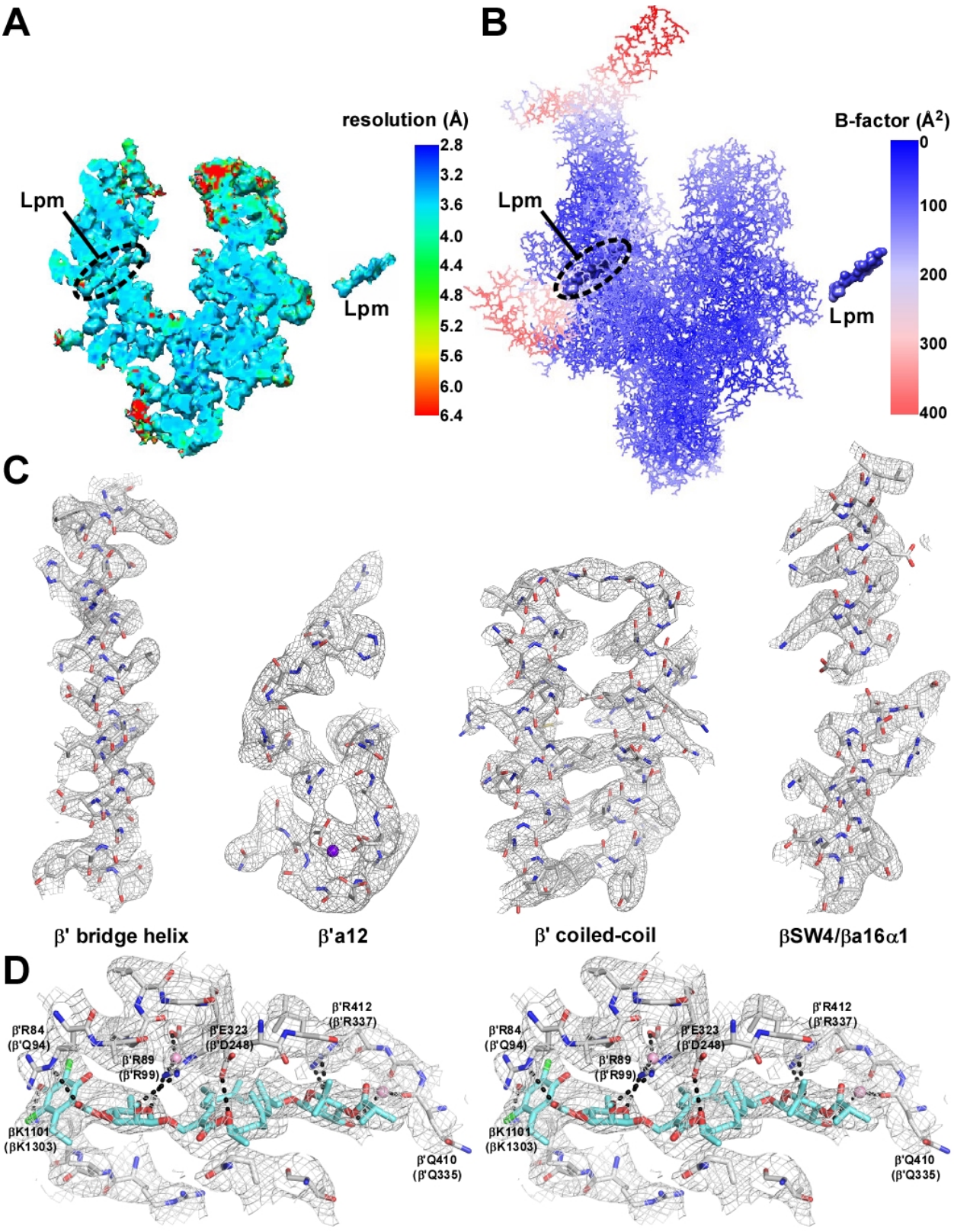
A
resolution (Å)
2.8
3.2
3.6
4.0
4.4
4.8
5.2
5.6
6.0
6.4
Lpm
Lpm
B
B-factor (Å²)
0
100
200
300
400
Lpm
Lpm
C
β' bridge helix
β'a12
β' coiled-coil
βSW4/βa16α1
D
β'R84 (β'Q94)
β'R89 (β'R99)
β'E323 (β'D248)
β'R412 (β'R337)
βK1101 (βK1303)
β'Q410 (β'Q335)
β'R84 (β'Q94)
β'R89 (β'R99)
β'E323 (β'D248)
β'R412 (β'R337)
βK1101 (βK1303)
β'Q410 (β'Q335)

Figure S2

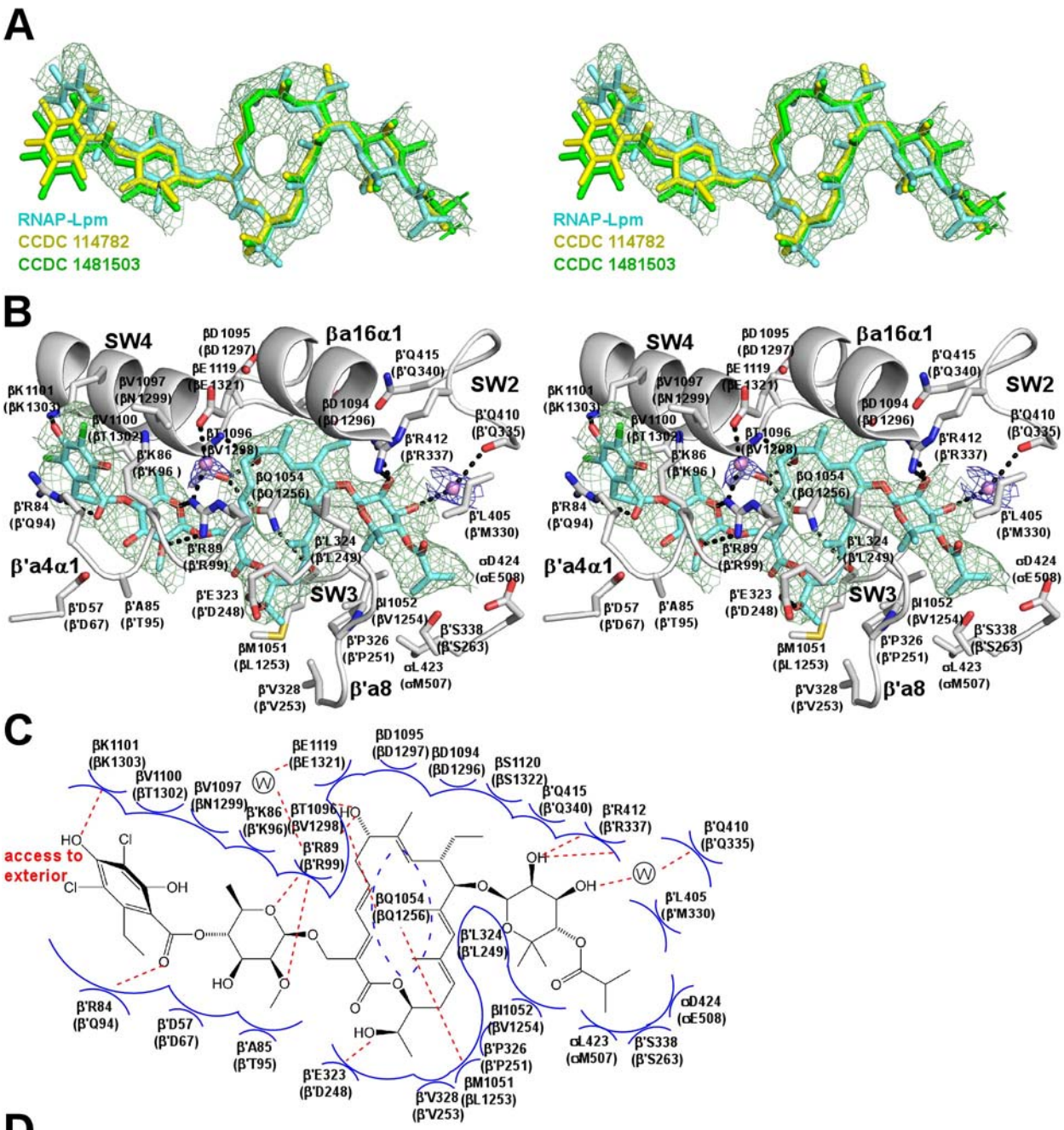

D

Effects of Ala substitution of RNAP residues that make H-bonds with Lpm

RNAP	Lpm-resistance ($IC50/IC50_{wild\text{-}type}$)
RNAP	1
[Ala1101 (1303)]β-RNAP	20
[Ala84 (94)]β'-RNAP	9
[Ala89 (99)]β'-RNAP	>400
[Ala323 (248)]β'-RNAP	40
[Ala412 (337)]β'-RNAP	>400

Figure S3

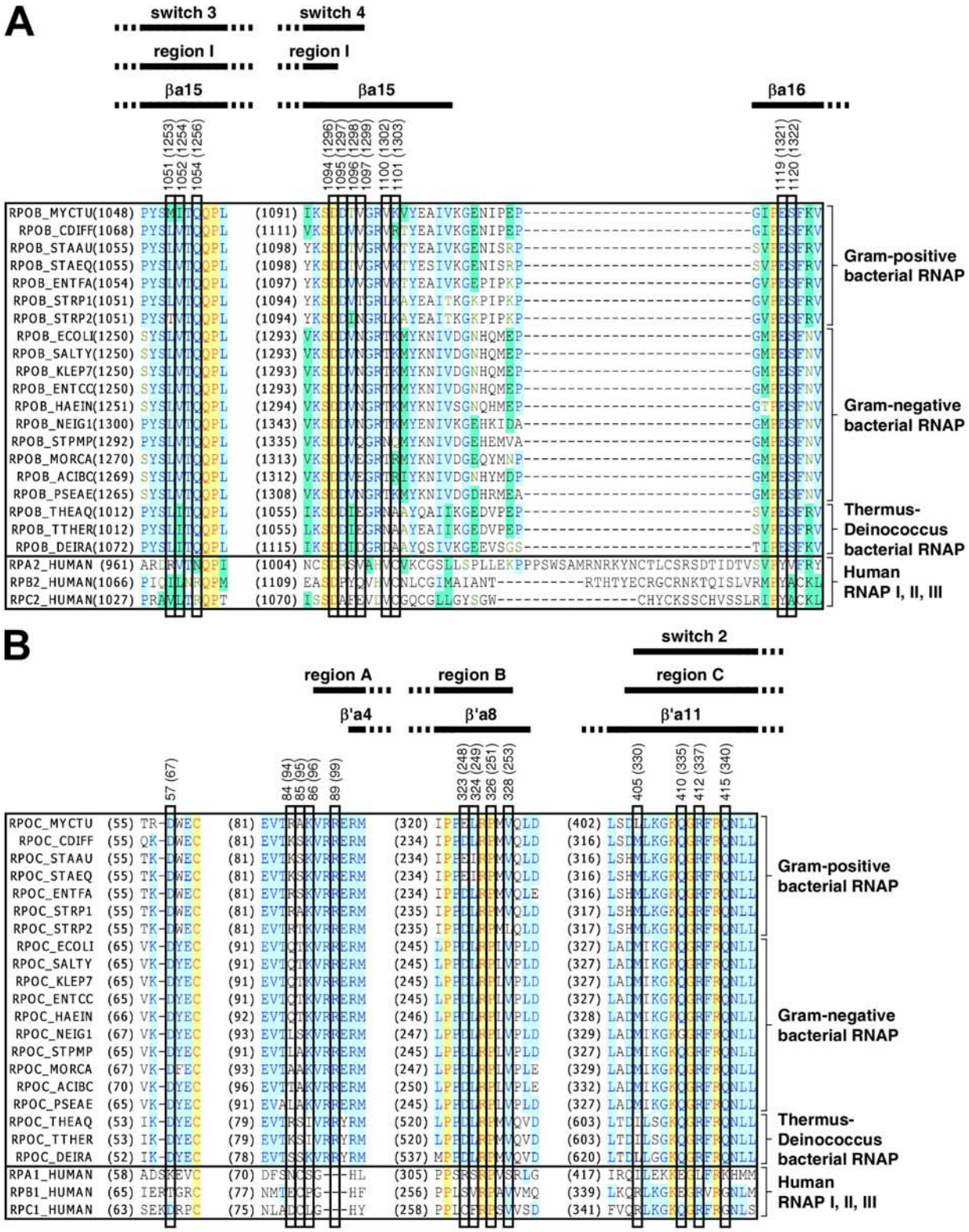

C Human RNAP I, II, and III: absence of inhibition by Lpm

RNAP	IC50 (μM)
HeLa nuclear extract (human RNAP I / II / III)	>400

Figure S4

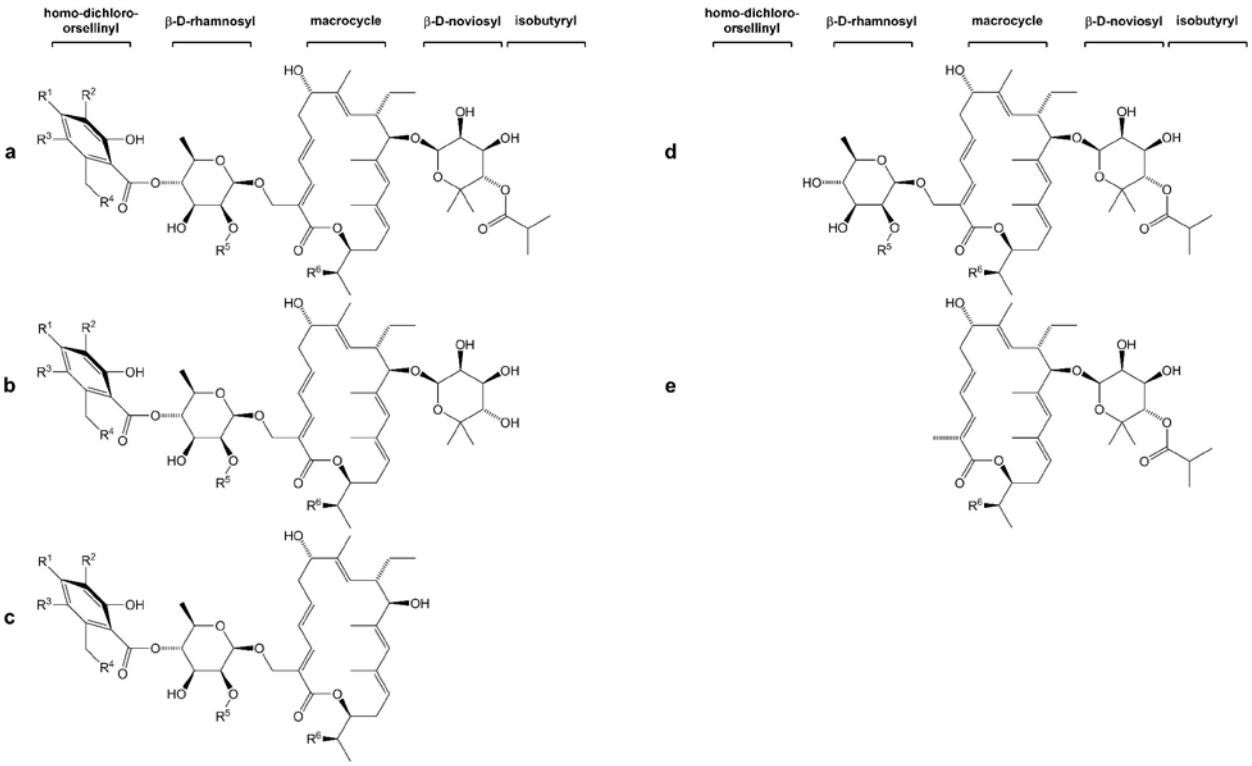

RNAP-inhibitory activity of Lpm analogs

compound	synonym(s)	R^1	R^2	R^3	R^4	R^5	R^6	relative RNAP-inhibitory activity ($IC50/IC50_{Lpm}$)		
								Mycobacterium tuberculosis RNAP	*Staphylococcus aureus* RNAP	*Escherichia coli* RNAP
Lpm	---	OH	Cl	Cl	CH_3	CH_3	OH	1	1	1
a1	4"-O-benzyl-Lpm (this work)	$O\text{-}CH_2\text{-}C_6H_5$	Cl	Cl	CH_3	CH_3	OH	20	5	1
a2	5"-deschloro-Lpm (this work)	OH	Cl	H	CH_3	CH_3	OH	10		
a3	3",5"-dideschloro-Lpm; 50-1d	OH	H	H	CH_3	CH_3	OH	10		
a4	5"-bromo-3",5"-dideschloro Lpm	OH	Br	H	CH_3	CH_3	OH	9		
a5	69-1d	OH	Cl	Cl	CH_3	CH_3	H	20		
a6	70-9d	OH	Cl	Cl	CH_3	H	OH	3		
a7	70-10d	OH	Cl	Cl	CH_3	H	H	50		
a8	70-11d	OH	Cl	Cl	H	H	OH	9		
b1	OP-1118	OH	Cl	Cl	CH_3	CH_3	OH	2		
b2	53-1d	OH	Cl	Cl	CH_3	CH_3	H	40		
c1	57-4d	OH	Cl	Cl	CH_3	H	H	300		
d1	desaryl-Lpm	---	---	---	---	CH_3	OH	>400		
e1	54-3d	---	---	---	---	---	H	>400		

Figure S5

A

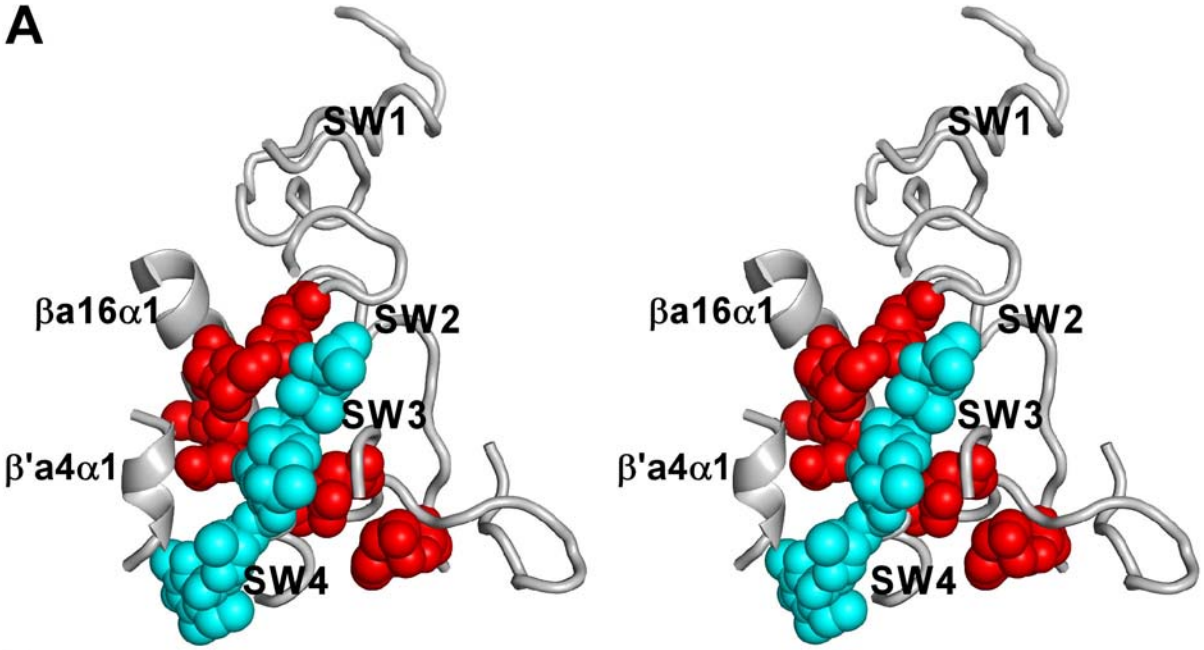

B

Lpm-resistant mutants: absence of significant cross-resistance to Myx, Cor, Rip, and Rif

amino acid substitution	location	cross-resistance level (MIC/MIC$_{wild\text{-}type}$)			
		Rif	Myx	Cor	Rip
rpoB **(RNAP β subunit)**					
811 (892) Glu→Ala	---	1	1	1	1
1049 (1251) Tyr→Phe	switch 3	1	0.5	0.5	1
1054 (1256) Gln→Glu	switch 3	1	1	0.5	1
1054 (1256) Gln→Leu	switch 3	1	1	1	0.5
1086 (1288) Gln→Leu	---	1	1	1	1
1095 (1297) Asp→Ala	switch 4	0.5	1	1	1
1095 (1297) Asp→Tyr	switch 4	0.5	1	1	1
1100 (1302) Thr→Pro	---	1	1	0.5	0.5
1117 (1319) Met→Arg	β a16	1	1	1	1
1117 (1319) Met→Ile	β a16	1	1	0.5	1
1117 (1319) Met→Lys	β a16	1	1	1	1
1119 (1321) Glu→Val	β a16	1	0.5	1	1
1122 (1324) Asn→Lys	β a16	1	1	1	1
1123 (1325) Val→Ala	β a16	1	1	1	1
1123 (1325) Val→Glu	β a16	1	1	1	1
1123 (1325) Val→Gly	β a16	1	1	1	1
1123 (1325) Val→Leu	β a16	1	1	1	1
rpoC **(RNAP β′ subunit)**					
86 (96) Lys→Ile	β′ a4	1	1	1	1
324 (249) Leu→Arg	β′ a8	1	1	1	1
338 (263) Ser→Thr	---	1	1	1	1
409 (334) Lys→Ile	switch 2	1	0.5	0.5	1
412 (337) Arg→His	switch 2	1	1	1	2
412 (337) Arg→Ser	switch 2	1	1	1	2
416 (341) Asn→Ser	switch 2	1	2	1	1
423 (348) Asp→Tyr	switch 2	1	1	1	1

C

Myx/Cor/Rip-resistant mutants: absence of significant cross-resistance to Lpm

amino acid substitution	cross-resistance level (MIC/MIC$_{wild\text{-}type}$)
rpoB **(RNAP β subunit)**	
1030 (1232) Met→Ile	1
1053 (1255) Thr→Ile	0.5
1073(1275) Val→Phe	0.5
1073(1275) Val→Met	0.5
1076 (1278) Leu→Val	1
1077 (1279) Glu→Gly	0.5
1077 (1279) Glu→Lys	1
1081 (1283) Ala→Val	0.5
1083 (1285) Tyr→Asp	1
1089 (1291) Leu→Phe	2
1096 (1298) Val→Leu	0.5
1113 (1315) Met→Leu	0.5
1115 (1317) Pro→Leu	1
1118 (1320) Pro→Ala	2
1120 (1322) Ser→Pro	0.5
1120 (1322) Ser→Thr	1
1120 (1322) Ser→Tyr	1
1120 (1322) Ser→Val	0.5
1124 (1326) Leu→Trp	0.5
rpoC **(RNAP β′ subunit)**	
420 (345) Lys→Arg	1
420 (345) Lys→Asn	0.5
420 (345) Lys→Gln	0.5
420 (345) Lys→Thr	0.5
1247 (1346) Gly→Asp	2
1252 (1351) Val→Phe	1
1253 (1352) Ile→Asn	1
1253 (1352) Ile→Ser	1
1255 (1354) Gly→Cys	4

Figure S6